Geophysical Journal International

Geophys. J. Int. (2026) **245,** 1–25
Advance Access publication 2026 April 15
Research paper

https://doi.org/10.1093/gji/ggag145

P- and *S*-wave speed evolution during rock deformation from coda wave interferometry and energy partitioning inversion

Jack-Andrew Smith [1], Maria-Daphne Mangriotis,[2] Andrew Curtis,[1] Xun Li,[1] Alexis Cartwright-Taylor,[3] Ian G. Main[1] and Ian B. Butler[1]

[1]*University of Edinburgh, Edinburgh, EH9 3FE, UK. E-mail: jack-andrew.smith@ed.ac.uk*
[2]*National Oceanography Centre, Southampton, SO14 3ZH, UK*
[3]*Heriot—Watt University, Edinburgh, EH14 4BA, UK*

Accepted 2026 April 13. Received 2026 April 3; in original form 2025 December 2

SUMMARY

Seismic wave speed monitoring is important for the non-destructive evaluation of material properties in response to external forcing. Coda wave interferometry (CWI) uses traveltime perturbations in multiply-scattered seismic wave trains—the seismic coda—to detect subtle perturbations in bulk wave speed. However, conventional body-wave CWI cannot separate the coupled contributions of *P* and *S* waves, which are sensitive to different material properties. We introduce *energy partitioning inversion* which decouples these modes by combining a scattering model with CWI measurements within non-equipartitioned coda windows. We applied this methodology to repeated ultrasonic pulse surveys during two laboratory loading experiments on Clashach sandstone: a dynamic experiment (constant strain rate until brittle failure) and a quasi-static experiment (modulating stress to maintain constant acoustic emission rate and slow down the failure process). Relative traveltime perturbations and their full covariance between all pairs of surveys were measured across multiple coda windows and inverted for a single perturbation profile using a least-squares method to minimize the variance of the profile. Using an isotropic point scatterer model to predict mode partitioning with respect to the coda lapse time, we invert traveltime perturbations for the scattering mean free path traveltime and relative *P* and *S* wave speed perturbations via Markov-chain Monte Carlo inversion to quantify uncertainty. *P* and *S* wave speed perturbations were resolved with 95 per cent credible intervals of 0.025 and 0.008 per cent, respectively. During the quasi-static experiment the temporal resolution was sufficient to capture a quasi-linear decrease in *P* and *S* wave speeds by ∼50 and ∼14 per cent, respectively, from peak to failure. The peak *P* and *S* wave speed perturbations were ∼33 per cent lower and ∼75 per cent higher, respectively, compared to those found in the dynamic experiment. These results demonstrate that CWI and energy partitioning inversion enables the robust, uncertainty-quantified evaluation of separate relative bulk *P*- and *S*-wave speed perturbations in strongly scattering media.

Key words: Fracture and flow; Interferometry; Inverse theory; Coda waves; Wave scattering and diffraction.

1 INTRODUCTION

The non-destructive evaluation of material integrity is critical for monitoring system responses to external forcing across an expansive range of scales and disciplines. Over the past several decades, changes in the velocity with which seismic or (an)elastic wavefields travel has served as a useful proxy for temporal variations in material density and (an)elastic moduli. Applications of velocity monitoring are now widespread: it is used in civil engineering to assess materials in buildings, bridges and earthen dams (M. Picozzi *et al.* 2011; S.C. Stähler *et al.* 2011; T. Planès *et al.* 2016); in subsurface industrial settings to monitor mining operations, geothermal energy production and large-scale reservoir characterization using time-separated seismic reflection surveys and passive seismic imaging (R.J. Arts *et al.* 2002; S.A.L. de Ridder & B.L. Biondi 2013; D.H. Johnston 2013; A. Obermann *et al.* 2015; G. Olivier *et al.* 2015); in environmental monitoring to capture seasonal changes due to precipitation, temperature changes, freeze-thaw cycles, long-term variations in climatic forcing and snow loading and melting (U. Meier *et al.* 2010; V.C. Tsai 2011; M. Gassenmeier *et al.* 2014; A. Mordret *et al.* 2016; T. Lecocq *et al.* 2017); in geophysical hazard assessment to monitor volcanic activity and stress-drops following the occurrence of earthquakes (U. Wegler & C. Sens-Schönfelder 2007; F. Brenguier *et al.* 2008, 2014); in industrial testing for flaws in manufactured components (K.M.M. Tant *et al.* 2018, 2020); in medical settings to characterize the elastic properties of muscle and the brain (K.G. Sabra *et al.* 2007;

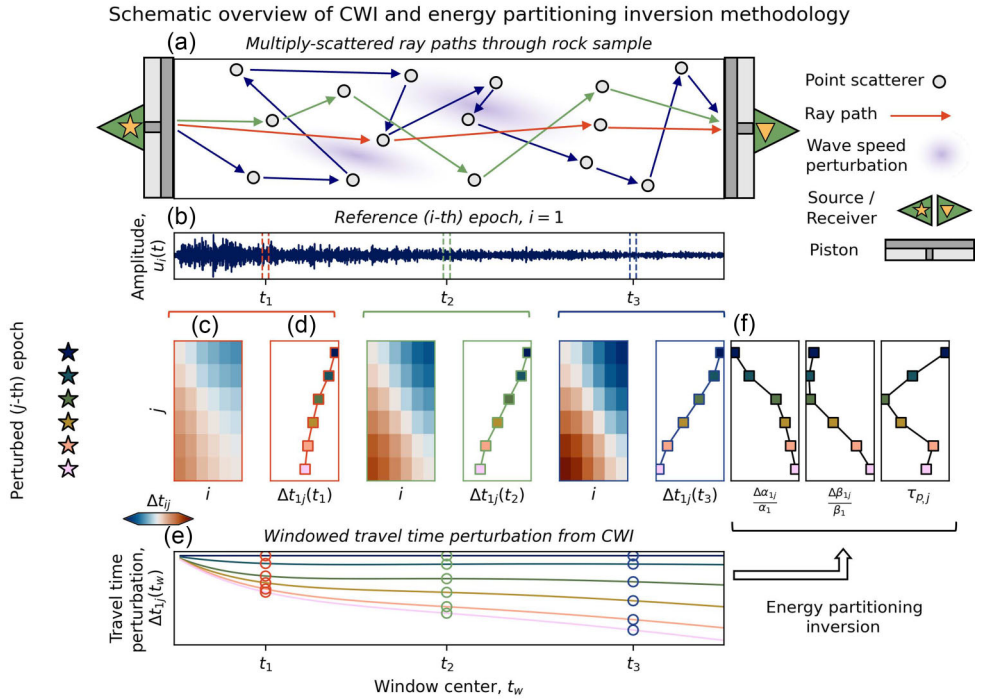

Figure 1. Summary of the energy partitioning inversion method. (a) Schematic of three possible ray paths (red, green, blue arrows) with successively longer traveltimes through a medium containing heterogeneities in rock materials represented by point scatterers and heterogeneous wave speed perturbations. (b) One active shot recording, with coda windows centred about lapse times t_1, t_2 and t_3, shown. (c) Traveltime perturbations Δt_{ij} between every pair of epochs i and j, within a single coda window around t_1, with delays in red and advances in blue. (d) A traveltime perturbation profile relative to a single reference epoch is calculated using a least-squares inversion of measurements in panel (c). Examples are also shown for coda windows around t_2 and t_3. (e) A traveltime perturbation profile similar to (d) is measured for all coda windows and displayed together. (f) Curves in panel (e) are used for energy partitioning inversion for the P and S wave speed perturbations relative to the first epoch, $\Delta\alpha_{1j}/\alpha_{ij}$ and $\Delta\beta_{1j}/\beta_{ij}$ respectively, and scattering mean free path traveltime $\tau_{p,j}$.

A. Zorgani *et al.* 2015); and in materials science to measure material responses to thermal, mechanical and other stimuli (R. Snieder *et al.* 2002; E. Larose & S. Hall 2009; T. Planès & E. Larose 2013).

Between repeated seismic surveys, changes in the bulk wave speed v, denoted Δv, manifest as changes in the traveltime t of seismic waves as they pass through the medium, denoted Δt. Conventionally, traveltime perturbations of the first arrival are used to infer changes in absolute wave speed, with many methods available for picking the first break of wave energy (R. Peraldi & A. Clement 1972; P.J. Hatherly 1982; C.P. Ervin *et al.* 1983; P.S. Earle & P.M. Shearer 1994; F. Boschetti *et al.* 1996; J.B. Molyneux & D.R. Schmitt 1999). However, first-break methods have three primary limitations: (1) Their spatial sensitivity is restricted to the specific paths through the medium that have close to the minimum possible traveltime, which may not represent bulk properties; (2) the exact ballistic path is poorly constrained and the assumption of a rectilinear ray path from source to receiver in heterogeneous media introduces a systematic bias towards lower apparent wave speeds (J. Singh *et al.* 2019); and (3) they are highly susceptible to noise (see Appendix A).

Rather than using the first arrival of energy, R.L. Weaver & O.I. Lobkis (2001) and O.I. Lobkis & R.L. Weaver (2001) demonstrated that meaningful information regarding relative bulk variations in the medium (e.g. $\Delta v/v$) can be extracted from the seismic coda—the multiply-scattered wave train following the first arrival of energy (K. Aki 1969). Coda waves provide a more complete sampling of the bulk medium in 3-D because they originate from multiply-scattered paths (Fig. 1a). They exhibit a higher sensitivity than the first-arrival to perturbations in pore pressure, fracture density and temperature (R. Snieder *et al.* 2002; S. Vlastos *et al.* 2006, 2007). Frequently, relative rather than absolute changes suffice to characterize the material response to external stimuli such as fluctuations in loading pressure (M. Landrø& J. Stammeijer 2004). Furthermore, as $|\Delta t|$ increases with path length for bulk-averaged wave speed changes, relative measurement errors are smaller when using coda waves rather than the first arrival, and values of $\Delta v/v$ can be estimated using a suite of techniques collectively termed *coda wave interferometry* (CWI).

When applying CWI to body waves, the relative proportion of P and S waves within the wavefield evolves with coda lapse time due to mode conversions that occur during scattering events, eventually approaching an equilibrium state with more S wave than P wave energy (R. Snieder 2002). Traditionally, CWI studies target this state by isolating late coda windows. However, the inability to distinguish between P and S wave speed variations represents a significant limitation of conventional techniques, as these modes exhibit distinct sensitivities to other specific material properties. For the first time using laboratory data, we demonstrate that P and S wave contributions to coda wave perturbations can be decoupled using non-equipartitioned coda windows in a step we refer to as *energy partitioning inversion*, building on the theoretical and synthetic work of R. Snieder (2002) and J. Singh *et al.* (2019), respectively.

Energy partitioning inversion relies on a scattering model; in this case, we apply an isotropic point scatterer model appropriate for strongly scattering media where wave speed perturbations are broadly distributed (R. Snieder 2002).

In this work, we infer relative perturbations in the bulk *P*- and *S*-wave speeds of a sandstone core during deformation in a laboratory using a sequence of repeated ultrasonic pulse surveys. Our methodology advances conventional CWI in three key areas: (1) We adapt the double wavelet CWI method of R. Snieder (2002) for measuring means and variances of $\Delta v/v$ between surveys by incorporating the covariance between survey pairs, ensuring correlations between CWI measurements are not neglected; (2) we minimize the variance of CWI measurements relative to the initial reference state by using a damped least-squares inversion of relative measurements between all survey pairs; and (3) we decouple the respective *P*- and *S*-wave contributions via energy partitioning inversion, also recovering the scattering mean free path traveltime—the average timescale for an initial packet of *P*-wave energy to convert to an *S* wave due to scattering. Our methodology operates within a fully probabilistic framework, allowing accurate uncertainty estimates that are essential for interrogating the wave speed evolution model for, for example, velocity thresholds marking transitions between deformation stages (R. Arnold & A. Curtis 2018).

We apply our methodology to two distinct laboratory loading configurations: A *dynamic* experiment where the sample is subjected to a constant strain rate until catastrophic failure, resulting in a sudden and sharp stress drop; and a *quasi-static* experiment in which the acoustic emission (AE) rate is maintained at a constant level by modulating the applied stress via AE feedback control, such that the stress drop is extended in a stable way with no dynamic failure (D.A. Lockner *et al.* 1991). Catastrophic failure in brittle, porous materials initiates when small fractures localize along an emergent shear band, transitioning from stable crack growth to unstable crack coalescence and dynamic rupture (D.A. Lockner *et al.* 1991). In the dynamic case, peak stress is typically accompanied by a rapid, non-linear acceleration of the AE rate (P.R. Sammonds *et al.* 1992), reflecting rapid fracture growth and coalescence (P.G. Meredith & B.K. Atkinson 1983) which severely limits the temporal resolution of measurements during the experiment relative to the duration of catastrophic failure.

Conversely, quasi-static experiments slow down the sample failure process (M. Terada *et al.* 1984). This approach allowed A. Cartwright-Taylor *et al.* (2022) to observe microstructural processes during failure, such as grain rolling, using X-ray imaging. Such aseismic deformation, usually representing the majority of accumulated strain energy (G. Dresen *et al.* 2020), is often detectable by velocity monitoring and is regarded as the largest source of uncertainty in induced seismic risk forecasting during subsurface fluid injection and extraction (S.J. Bourne *et al.* 2014). We find that using an acoustic emission control to slow down the deformation process changes the evolution of bulk mechanical properties of the medium in the lead up to brittle failure, which should be considered when setting seismic velocity thresholds for risk management of material integrity (R.J. Walters *et al.* 2015; G.R. Foulger *et al.* 2018).

2 MATERIALS AND METHODS

2.1 Data

We use repeated active seismic surveys (Section 2.1.2) which were taken at a constant time interval throughout two rock deformation experiments (Section 2.1.1)—a dynamic experiment (A) and quasi-static experiment (B) (A. Cartwright-Taylor *et al.* 2022)—with a Clashach sandstone sample. Experiments A and B are the same as those analysed by M.D. Mangriotis *et al.* (2025) with identical corresponding labels.

2.1.1 Experimental setup

The experimental material was a highly cemented (17 per cent porosity) quartz-rich sandstone from the Clashach quarry in Morayshire, Scotland, cut to cylindrical cores of 10 mm in diameter and 25 mm in length (Fig. 2). The samples were saturated with deionized water and subjected to triaxial deformation in a pressure vessel called Stór Mjölnir (Fig. 2a), developed by I. Butler *et al.* (2020) and A. Cartwright-Taylor *et al.* (2022). Both experiments were conducted at room temperature and the Clashach cores were jacketed in silicone tubing with a confining pressure of 25 MPa and a pore fluid pressure of 5 MPa, which was maintained throughout the test. Initially, a hydrostatic pressure starting condition was produced by increasing the axial pressure to match the confining pressure, before the principal loading of the sample axially by fluid injection to the hydraulic actuator.

Two Glaser-type *P*-wave piezoelectric transducers (G.C. McLaskey & S.D. Glaser 2012) were positioned axially on the ends of the pistons (Figs 2b and c). The transducers have a flat response spectrum between 500 kHz and 2 MHz, measuring normal displacement, with a contact area of 0.5 mm diameter. A smear of high-viscosity molasses was used to couple the transducers to the pistons and silicone grease was used between the pistons and ends of the sample.

During the dynamic experiment (A), the sample was strained at a constant strain rate of $10^{-5}\,\mathrm{s}^{-1}$ until brittle failure (Fig. 3b). During the loading period, the corresponding axial load response showed behaviour typical of brittle deformation: early nonlinear, transitioning into linear and then to nonlinear again (Fig. 3a). These regions were associated with early compaction, competing compaction and dilation/shear, and dilation-/shear-dominant processes, respectively (M.D. Mangriotis *et al.* 2025). Acoustic emissions (AE)

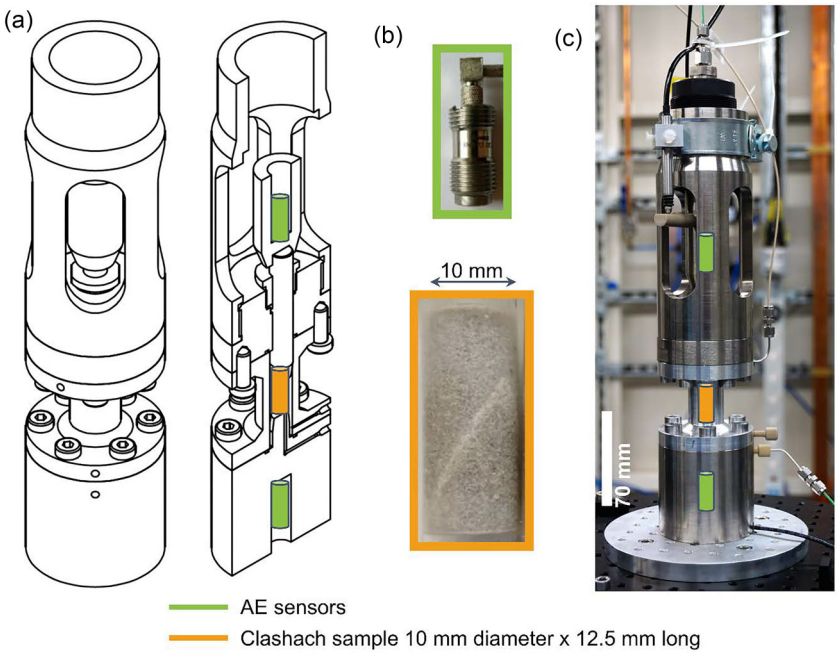

Figure 2. (a) Schematic of the X-ray transparent deformation rig, Stór Mjölnir (A. Cartwright-Taylor *et al.* 2022). (b) During the loading experiment, two Glaser-type *P*-wave piezoelectric transducers (top) send and receive ultrasonic pulses through a sample of Clashach sandstone (bottom). (c) The transducers (green cylinders, top and bottom) are positioned axially on the ends of pistons which subject the sample (orange cylinder, middle) to triaxial deformation.

were produced by microscopic processes as the rock deformed and were counted when the amplitude of the events exceeded a user-set threshold. Just prior to failure, the AE count accelerated and the sample underwent runaway catastophic failure (Fig. 3d).

In the quasi-static experiment (B), the applied stress was modulated after the yield point (Fig. 3f) by an AE event rate servo-control, by slowing down the stroke rate of the ram, or allowing it to go into reverse, in order to maintain an average AE rate of $1 \pm 1\,\mathrm{s}^{-1}$ measured over intervals of 10 s (Fig. 3d). As a consequence, the length of time for strain softening and fault formation was extended from ∼1 to ∼50 min, allowing for greater relative temporal resolution of observations with respect to the duration of the failure window (D.A. Lockner *et al.* 1991, 1992).

Although both cores were taken from the same block of material, geological heterogeneity results in measurable differences between the samples in work done prior to yield despite the test protocols being identical until this point (Fig. 3c). Experiment B required greater mechanical work than experiment A, indicating that the former sample was stiffer, underwent less compaction before entering the quasi-elastic regime and experienced a higher peak differential stress after yield.

2.1.2 Seismic data

The acoustic transducers act as both sources and receivers of ultrasonic *P* waves using the pulse transmission technique (F. Birch 1960). Ultrasonic active surveys were conducted every 5 min during loading for both experiments (Fig. 3e). To improve signal-to-noise, ten shots were taken in short succession during each active survey and stacked. We refer to each survey as an *epoch* (see Table 1 for a summary of time variable nomenclature). Although two active shots were taken at each epoch with the top and bottom acoustic transducers as sources, respectively, continuous data acquired at 10 MHz with a long enough recording window to capture the full seismic coda was only recovered from the top transducer with the bottom transducer as a source.

The source time of each survey was measured by manual inspection for the first-break in the voltage output of the source transducer, and traces further aligned using cross-correlation of the electrical shock noise which propagates through the deformation rig and arrives before the seismic signal (amplitude spike in Figs 4a and d). A subsequent systematic correction was made to the source time to account for the propagation duration through the pistons, measured by an active survey with no sample placed in the pressure vessel and the pistons clamped together.

Although the first arrival time is <10 μs, the coda lasts for over 1200 μs with a logarithmic decay in instantaneous power (Fig. 4a). The exact first arrival time is not obvious, and no clear *S* wave arrival is identifiable (Fig. 4e). However, traveltime perturbations between epochs are clearly discernible when comparing the coda of the waveforms at different epochs (Figs 4f and g). There is a significant decrease in the signal-to-noise ratio above 1.0 MHz, and the dominant frequency is <0.4 MHz in the early coda before stabilizing to ∼0.6 MHz in the late coda (Fig. 4b).

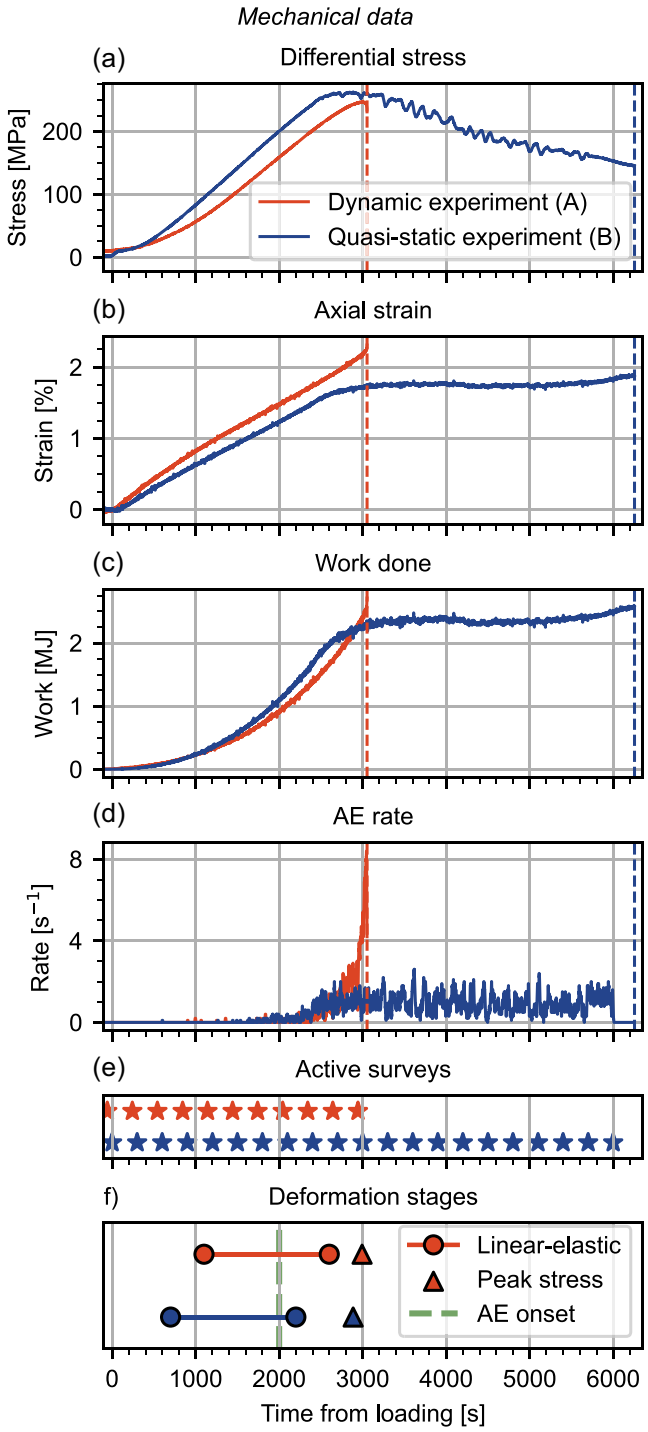

Figure 3. (a) Profile of the differential stress evolution, (b) profile of the axial strain evolution and (c) subsequent work done calculated by integrating the stress–strain curve during the dynamic (A, red) and quasi-static (B, blue) experiments. (d) The AE rate was held at $1 \pm 1\ s^{-1}$ during experiment B to slow down the deformation process. (e) Active seismic surveys were taken approximately every 5 min. (f) The linear-elastic deformation regime begins after the loading onset and ends at the yield point, before reaching peak stress. The vertical dashed lines in panels (a)–(d) represent the time of failure during experiment A and the end of loading in experiment B.

Table 1. Nomenclature and definitions for temporal variables.

Epoch	Index of each active source seismic survey during the experiment
Traveltime	Duration of travel from source to receiver for a specific seismic phase during an active survey
Lapse time	Time elapsed since the active survey source time
Coda window	A window over lapse time
Lag time	Time-shift in cross-correlation of coda windows between epochs

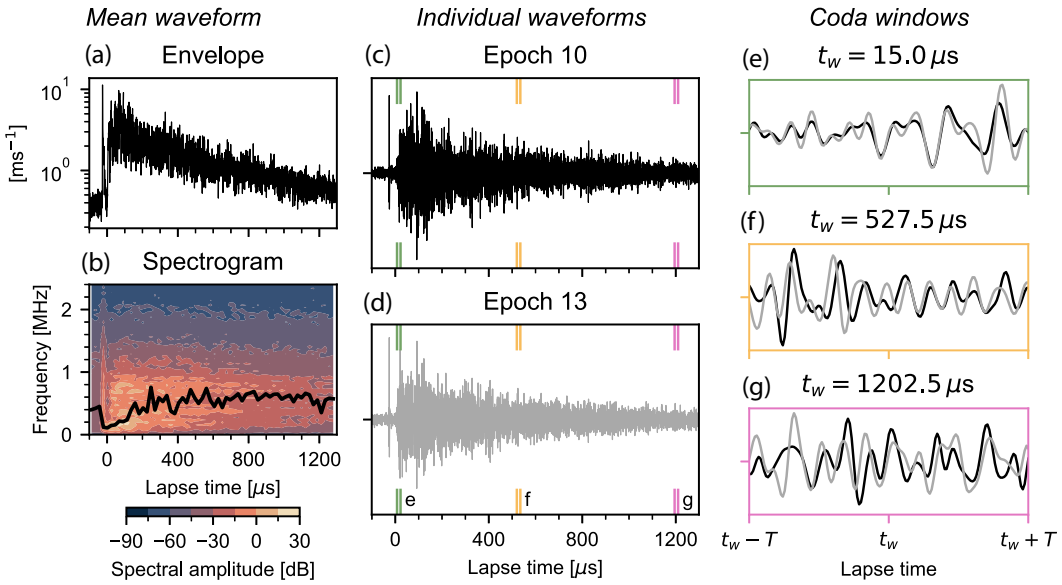

Figure 4. Recorded waveform examples from dynamic experiment (A). (a) Mean amplitude envelope and (b) spectrogram (dominant frequency as solid line) over all epochs. Recorded waveforms at epochs (c) 10 (black) and (d) 13 (grey). Traveltime perturbations are slight in early coda windows, for example, (e) central time 15.0 μs and more pronounced in later coda windows, for example, central times (f) 527.5 μs and (g) 1202.5 μs. Coda windows have half-width $T = 15$ μs.

2.2 Background theory

In Sections 2.2.1 and 2.2.2, we provide the necessary background to set up two respective inversions. First, we describe the theory for the CWI double wavelet method for estimating means and variances of relative traveltime perturbations between pairs of epochs within a coda window (R. Snieder 2006). These measurements are used in the first inversion for a traveltime perturbation profile relative to a single reference epoch (Figs 1c and d, Section 2.4). Then, we describe the scattering model used to obtain relative changes in the *P* and *S* wave speeds from the aforementioned traveltime perturbation profiles during the second inversion–energy partitioning inversion (Figs 1e and f, Section 2.5). We refer the reader to Table 1 for a summary of time variable nomenclature.

We show how to obtain the full covariance structure for measurements of relative traveltime perturbations, assuming errors in coda waveforms are uncorrelated between epochs. This covariance structure propagates into that of the traveltime perturbation profiles during the first inversion, which in turn propagates into the covariance structure of the *P*- and *S*-wave speed perturbation profiles during the second inversion (energy partitioning inversion). If correlations within the input to either inversion are ignored, then inputs are falsely treated as providing independent information and therefore maximum constraint on the output, such that the uncertainty on the output will be underestimated.

2.2.1 Coda wave interferometry

The average wave speed perturbation Δv between epochs i and j along ray path P within a medium is denoted $\Delta v_{ij,P}$. The corresponding traveltime perturbation Δt along path P is

$$\Delta t_{ij,P} = -\frac{\Delta v_{ij,P}}{v_{i,P}} t_{i,P} \tag{1}$$

where $t_{i,P}$ is the traveltime and $v_{i,P}$ the average velocity during epoch i along path P, assuming the path length remains unchanged between epochs i and j (R. Snieder 2002). The relative change in path length due to the applied strain by pistons is assumed to be negligible as the path length of arrivals in the coda is much larger than the dimensions of the sample. Waves arriving later in the coda (i.e. larger $t_{i,P}$) are multiply-scattered and hence sample the medium over a larger volume and range of propagation directions. Therefore, as $t_{i,P}$ increases, $\Delta v_{ij,P}$ approaches the bulk average isotropic wave speed perturbation, Δv_{ij}.

Although one cannot measure traveltime perturbations along individual ray paths P, which are unknown, *R*. Snieder (2002) showed how to extract the first and second moments of the associated Δt distribution for a set of arrivals within a coda window of width $2T$ about a central time t_w using the *double wavelet* method. They use the windowed cross-correlation function, R_{ij} between the seismic recording at epoch i, $u_i(t)$, and the seismic recording at epoch j, $u_j(t)$

$$R_{ij}(\tau; t_w, T) = \frac{\int_{t_w-T}^{t_w+T} u_i(t')\, u_j(t'+\tau)\, dt'}{\int_{t_w-T}^{t_w+T} u_i^2(t')\, dt'}, \tag{2}$$

where τ is the lag time of the cross-correlation function. We denote the expectation and variance of the traveltime perturbation distribution for arrivals within the window as

$$\langle \Delta t_{ij} \rangle \equiv \left\langle \left\{ \Delta t_{ij,P} \right\}_{t_{i,P} \in [t_w - T, t_w + T]} \right\rangle \tag{3}$$

and

$$\mathrm{var}\left(\Delta t_{ij}\right) \equiv \mathrm{var}\left(\left\{ \Delta t_{ij,P} \right\}_{t_{i,P} \in [t_w - T, t_w + T]} \right) , \tag{4}$$

respectively, where $\left\{ \Delta t_{ij,P} \right\}_{t_{i,P} \in [t_w - T, t_w + T]}$ is the set of traveltime perturbations $\Delta t_{ij,P}$ along all the different ray paths P which arrive within the coda window in square brackets and notation about the dependence of $\langle \Delta t_{ij} \rangle$ and $\mathrm{var}\left(\Delta t_{ij}\right)$ on t_w and T is omitted. As derived by R. Snieder (1986), the expected value of the Δt distribution is approximated by

$$\langle \Delta t_{ij} \rangle = \tau_{ij}^{\max}, \tag{5}$$

where $\tau_{ij}^{\max}$ is the lag time τ corresponding to the maximum of the cross-correlation function (eq. 2) and hence can be measured. The relationship between the variance and the maximum cross-correlation value is approximately given by

$$R_{ij}\left(\tau_{ij}^{\max}; t_w, T\right) = 1 - \frac{1}{2} \bar{\omega}_i^2 \mathrm{var}\left(\Delta t_{ij}\right) , \tag{6}$$

where $\bar{\omega}_i^2$ is the dominant mean square angular frequency of windowed $u_i(t)$ given by

$$\bar{\omega}_i^2 = \frac{\int_{t_w - T}^{t_w + T} \dot{u}_i^2(t') \, \mathrm{d}t'}{\int_{t_w - T}^{t_w + T} u_i^2(t') \, \mathrm{d}t'}, \tag{7}$$

where Newton's overdot notation is used to represent the time derivative (R. Snieder 2002).

The covariance of the Δt distribution between two pairs of epochs, $\{i, j\}$ and $\{k, l\}$, is not necessarily equal to zero if there is a common shot recording used in both measurements, that is, any of $\{i, j\}$ are equal to any of $\{k, l\}$. The covariance, $\mathrm{cov}\left(\Delta t_{ij}, \Delta t_{kl}\right)$, can be calculated from the formula for the variance of a sum,

$$\mathrm{var}\left(A \pm B\right) = \mathrm{var}\left(A\right) + \mathrm{var}\left(B\right) \pm 2\mathrm{cov}\left(A, B\right) , \tag{8}$$

and the following identities:

$$\Delta t_{kl} - \Delta t_{ij} = \begin{cases} \Delta t_{jl} & \text{for} \quad (i = k) \cap (j \neq l) \\ \Delta t_{ki} & \text{for} \quad (i \neq k) \cap (j = l) \end{cases} \tag{9}$$

$$\Delta t_{kl} + \Delta t_{ij} = \begin{cases} \Delta t_{kj} & \text{for} \quad (i = l) \cap (j \neq k) \\ \Delta t_{il} & \text{for} \quad (i \neq l) \cap (j = k) \end{cases} \tag{10}$$

$$\Delta t_{ij} = \begin{cases} \Delta t_{kl} & \text{for} \quad (i = k) \cap (j = l) \\ -\Delta t_{kl} & \text{for} \quad (i = l) \cap (j = k) \end{cases} . \tag{11}$$

Combining eqs (8), (9), (10) and (11), the covariance can be calculated by

$$\begin{aligned} \mathrm{cov}\left(\Delta t_{ij}, \Delta t_{kl}\right) = \frac{1}{2} \big[&\left(\delta_{ik} \vee \delta_{jl}\right) - \left(\delta_{il} \vee \delta_{jk}\right) \big] \\ &\times \big[\mathrm{var}\left(\Delta t_{ij}\right) + \mathrm{var}\left(\Delta t_{kl}\right) \\ &- \left(\delta_{ik} \mathrm{var}\left(\Delta t_{jl}\right) + \delta_{jl} \mathrm{var}\left(\Delta t_{ki}\right)\right) \\ &+ \delta_{il} \mathrm{var}\left(\Delta t_{kj}\right) + \delta_{jk} \mathrm{var}\left(\Delta t_{il}\right)\big) \big] , \end{aligned} \tag{12}$$

where $\vee$ denotes the logical disjunction such that $a \vee b = 1$ if a and/or b are 1. Note that $\mathrm{var}\left(\Delta t_{nn}\right) = 0$ for $n \in \{i, j, k, l\}$.

Using eqs (5), (6) and (12), the cross-correlation function between recordings of active shots at different epochs can enable us to interpret waveform changes between epochs as the distribution of traveltime perturbations of waves arriving within a coda window. These traveltime perturbations are caused by the relative wave speed perturbation $\Delta v/v$ within the medium that occurs between epochs, where the expected value of $\Delta v/v$ is

$$\frac{\langle \Delta v_{ij} \rangle}{v_i} = -\frac{\langle \Delta t_{ij} \rangle}{t_w} . \tag{13}$$

Consequently, one can use multiple coda windows (i.e. different t_w) to estimate $\Delta v/v$. Under the principle of linear elasticity, waves travelling along different ray paths are independent from one another and therefore estimates of $\Delta v/v$ from eq. (13) are independent if calculated from non-overlapping time windows.

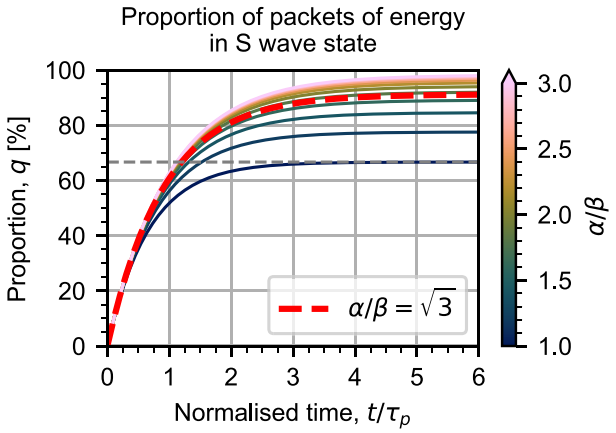

Figure 5. The proportion q of packets in an S-wave state increases with lapse time t normalized by the scattering mean free path traveltime τ_p, with the rate of increase and the equilibrium value of q determined by α/β. The equilibrium value for $\alpha/\beta = 1$ is $q = 2/3$, marked by the black horizontal dashed line. A Poisson's solid is marked by the red dashed line.

2.2.2 P- and S-wave energy partitioning

If the waveform energy comprised only a single wave type, independent estimates of $\Delta v/v$ from eq. (13) using measurements from windows throughout the coda would all approximate the same value. However, due to mode conversions during multiple scattering between source and receiver in the 3-D elastic experimental domain, the waveform energy consists of P wave energy travelling in one mode at speed α and S-wave energy travelling in two modes with different polarizations at speed β, with relative wave speed perturbations of $\Delta\alpha/\alpha$ and $\Delta\beta/\beta$, respectively. Consequently, estimates of $\Delta v/v$ contain information about both $\Delta\alpha/\alpha$ and $\Delta\beta/\beta$.

The scattering model of R. Snieder (2002) provides a way of decoupling $\Delta\alpha/\alpha$ and $\Delta\beta/\beta$ from estimates of $\Delta v/v$ for a medium of constant wave speed containing simplified heterogeneities acting as an isotropic set of point scatterers. Wave propagation is modelled as many packets of energy in either a P- or S-wave mode and can only be in one mode at a time. At each point scatterer, a packet of P-wave energy has probability p_{PS} of converting to a packet of S -wave energy, and likewise a packet of S-wave energy has probability p_{SP} of converting to a packet of P-wave energy. Over a lapse time interval $\mathrm{d}t$, a packet of P-wave energy encounters $\alpha \mathrm{d}t/a$ scatterers on average, where a is the average distance between point scatterers, and likewise a packet of S-wave energy encounters $\beta \mathrm{d}t/a$ scatterers on average. As $\alpha > \beta$, a packet of P-wave energy is likely to encounter more point scatterers in the time interval $\mathrm{d}t$ than a packet of S-wave energy. This effect will be amplified as α/β increases. Because packets of P-wave energy encounter more scatterers within a given time interval and there are more S-wave modes than P-wave modes, the wave energy will become dominated by S-wave energy with increasing traveltime of the wavefield.

R. Snieder (2002) derives the following system of differential equations for the rate of change of number of packets of P-wave energy, N_P, and number of packets of S-wave energy, N_S:

$$\dot{N}_P = \frac{1}{a}\left(p_{SP}\,\beta N_S - 2p_{PS}\,\alpha N_P\right) \tag{14}$$

$$\dot{N}_S = \frac{1}{a}\left(p_{PS}\,\alpha N_P - p_{SP}\,\beta N_S\right). \tag{15}$$

By assuming the medium is non-attenuative, that all the packets of energy begin in the P-wave state, that is, the source is purely compressional, and $p_{SP}/p_{PS} = (\beta/\alpha)^2$ (L. Margerin *et al.* 2000), these differential equations can be solved for the relative proportion of packets of S waves at time t (see Appendix B)

$$q(t) = \frac{N_S}{N_P + N_S} = \frac{1}{\gamma}\left(1 - e^{-\gamma t/\tau_p}\right), \tag{16}$$

where

$$\gamma = \frac{1}{2}\left(\frac{\beta}{\alpha}\right)^3 + 1, \tag{17}$$

and where τ_p is the scattering mean free path traveltime ($\tau_p = l_p/\alpha$ where $l_p = a/2p_{PS}$), that is, the average timescale for an initial packet of P-wave energy to convert to an S wave due to scattering. The relative proportion of packets of S waves converges to $1/\gamma$ as the traveltime increases and the energy partitioning of the wavefield is in equilibrium (Fig. 5). During the period in which the energy partitioning is evolving from some initial ratio of P- to S-wave energy towards equilibrium, the wavefield is described as being in *ringdown mode* (R. Snieder & M. Deheuvels 2024).

The predicted $\Delta v/v$ can therefore be decomposed into its *P*- and *S*-wave components:

$$\left[\frac{\Delta v_{ij}}{v_i}\right](t) = (1 - q(t))\frac{\Delta\alpha_{ij}}{\alpha_i} + q(t)\frac{\Delta\beta_{ij}}{\beta_i} \tag{18}$$

and corresponding Δt:

$$\Delta t_{ij}(t) = -t\left[(1 - q(t))\frac{\Delta\alpha_{ij}}{\alpha_i} + q(t)\frac{\Delta\beta_{ij}}{\beta_i}\right]. \tag{19}$$

Conventional CWI only uses late coda windows whereby $\Delta v/v$ is lapse time-invariant as energy has equilibrated, but J. Singh *et al.* (2019) showed that the nonlinearity of Δt measurements with lapse time in ringdown mode can be used to separate $\Delta\alpha/\alpha$ and $\Delta\beta/\beta$ by using the sensitivity kernel $q(t)$. Eq. (19) is a nonlinear equation linking measurements of the traveltime perturbation Δt at multiple lapse times t to the *P*-wave speed perturbation $\Delta\alpha/\alpha$, *S*-wave speed perturbation $\Delta\beta/\beta$, scattering mean free path traveltime τ_p and *P*-to-*S* wave speed ratio α/β. We solve eq. (19) for the latter four parameters using the Metropolis–Hastings Markov chain Monte Carlo algorithm (K. Mosegaard & A. Tarantola 1995; A. Malinverno & S. Leaney 2000), described in Section 2.5.

2.3 Traveltime perturbation measurements

The traveltime perturbation of an arrival along path *P*, $\Delta t_{ij,P}$, is estimated by the Δt distribution within a coda window with central time $t_w = t_{i,P}$ (Fig. 1b), using the double wavelet method (Section 2.2.1). First, a bandpass filter was applied to the signals, with low- and high-corner frequencies 0.4 and 1.0 MHz, respectively, retaining estimated wavelengths of 3.92–9.80 mm for *P* waves and 2.58–6.45 mm for *S* waves in Clashach sandstone (C. MacBeth 2004). The high corner of the frequency band is chosen to maximize signal-to-noise, which decreases at higher frequencies (Fig. 4b). Random, incoherent noise decreases the correlation coefficient in CWI measurements, which we do not account for. The low-corner frequency ensures estimated wavelengths are smaller than the dimensions of the sample to provide sensitivity to scatterers within the medium.

The mean and covariance of traveltime perturbations within windowed recordings between two epochs were found using the maximum of the cross-correlation function (eqs 5, 6 and 12). The coda window length was 15.0 μs with a 2.5 μs cosine taper applied to each end so that the central untapered 10.0 μs constitutes four periods at the low-corner frequency. The cosine taper reduces edge effects in the cross-correlation function due to the Gibbs phenomenon (J.W. Cooley & J.W. Tukey 1965). Multiple windows were used throughout the coda, with a 12.5 μs spacing so that only the tapered part of the windows overlapped. The windowed cross-correlation function contains both the cross-correlation of waves along common paths and cross-terms associated with the cross-correlation of waves that have travelled along different paths. The amplitude of the cross-terms relative to the desired diagonal terms is $\sim 1/\sqrt{n}$ where n is the number of degrees of freedom in the signal, which is in turn equal to the product of the bandwidth and window length (H.J. Landau 1967; O.M. Bucci & G. Franceschetti 1989; R. Snieder 2004) giving a relative amplitude in our study of around 24 per cent. This could be decreased if a greater window size were used, however fewer independent measurements would then be available through the coda.

The correct local maxima in the cross-correlation function must be chosen so that arriving waves are correctly matched between the reference and perturbed epochs. Cross-correlation functions with multiple local maxima (e.g. Figs 6a and b) can lead to the incorrect matching of waveforms, that is, cycle skipping. This problem is more severe for waveforms with a high-dominant frequency. Therefore, in order to build a Δt profile across all perturbed epochs relative to a particular reference epoch, we used a practice borrowed from full-waveform inversion (C. Bunks *et al.* 1995), whereby we began with low-frequency measurements and incrementally expanded the bandwidth to higher frequencies. A Tukey window was applied in the frequency domain with a fixed low-corner frequency and variable high-corner frequency defining the flat-top boundaries of the filter, with one-octave cosine tapers. The initial signal was narrow-band, with coincident high- and low-corner frequencies. The correct local maxima to pick for the autocorrelation function at the reference epoch is at zero lag. For the cross-correlation function between the reference epoch and a perturbed epoch, the correct local maxima will be the closest to zero lag if Δt is smaller than the dominant wavelength. Therefore, the local maxima chosen for cross-correlation functions between the reference epoch and adjacent epochs in experimental time was the closest to zero lag. Iteratively, the local maxima for other epochs were selected as the maxima with the closest lag time to the neighbouring epoch (Fig. 6c). Then, the high-corner frequency of the bandpass was increased, and the measured Δt profile was updated to consist of local maxima in the cross-correlation functions with lag closest to the measured Δt profile using the previous bandpass filter (Fig. 6d). This latter process was iterated until the full frequency range was applied to the signals.

2.4 Traveltime perturbation profiles

Within a single coda window, we calculated the mean and covariance of Δt distributions between all possible pairs of epochs, $\{i, j\}$ and $\{k, l\}$ for $i, j, k, l \in \{1, 2, \ldots, N\}$, denoted $\langle\Delta t_{ij}\rangle$ and $\mathrm{cov}(\Delta t_{ij}, \Delta t_{kl})$, respectively. To interpret the Δt profile throughout the experiment, one must find the Δt distribution relative to a single reference state, chosen to be epoch 1. The Δt profile relative to epoch 1 is written as

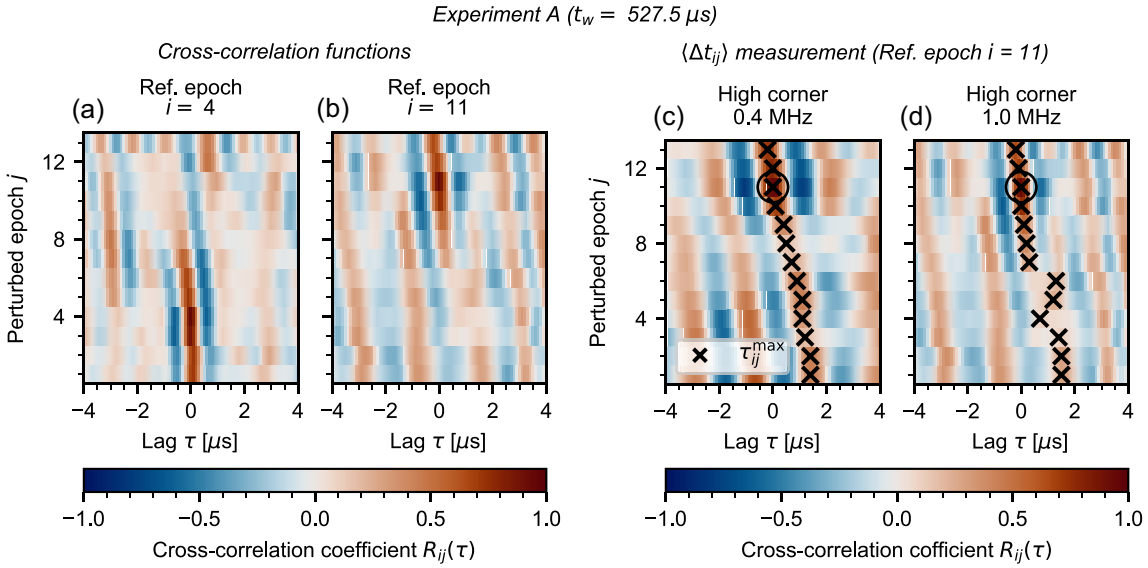

Figure 6. Cross-correlation functions from the recording of the active survey at the reference epoch [the i-th epoch, (a) $i = 4$ and (b) $i = 11$] to recordings at every epoch in the series (the j-th epoch) in a coda window centred at lapse time 527.5 μs during the dynamic experiment (A). Then, selecting the local maxima for, for example, $i = 11$ to measure the mean traveltime perturbation by gradually increasing the upper corner of the bandpass filter (c–d). The correct local maxima for the autocorrelation is at zero lag (circled).

a vector $\mathbf{m} = \left[\langle \Delta t_{1j} \rangle\right]$, with covariance matrix $Q_{\mathbf{m}} = \left[\mathrm{cov}\left(\Delta t_{1j}, \Delta t_{1l}\right)\right]$. An estimate $\hat{\mathbf{m}}$ of $\mathbf{m}$ can be found using various combinations of relative measurements with different reference epochs.

The simplest way to build a traveltime perturbation profile relative to the fixed reference epoch 1 is to use direct measurements of the Δt distribution between reference epoch 1 and all other epochs. This is called the *fixed reference* method. An assumption underlying the CWI method for estimating $\Delta v/v$ is that there are no changes in the ray paths. However, during rock deformation, scatterers are moved, new scatterers are created and old scatterers are destroyed during the closure of pore spaces, addition of microcracks and coalescence of fractures and all of these effects can change ray paths. When there are changes in the ray paths, the waveform may or may not be shifted in time significantly but the waveform shape will be distorted. This is turn will reduce the correlation coefficient between time-shifted waveforms recorded at different epochs, making it more difficult to match the corresponding wave phases between epochs. Therefore, relative measurements between epochs far apart in experimental time, between which the medium has changed substantially, will be less reliable. To limit the extent of these changes, the *moving reference* method may be used, whereby the Δt profile is built up by accumulating Δt measurements between epochs adjacent in experimental time:

$$[\hat{\mathbf{m}}_{\mathrm{MR}}]_j = \sum_{p=2}^{j} \langle \Delta t_{(p-1),p} \rangle \tag{20}$$

$$\left[Q_{\hat{\mathbf{m}}_{\mathrm{MR}}}\right]_{jl} = \sum_{p=2}^{j} \sum_{q=2}^{l} \mathrm{cov}\left(\Delta t_{(p-1),p}, \Delta t_{(q-1),q}\right) . \tag{21}$$

Note that using the moving reference method results in the accumulation of error throughout the Δt profile (eq. 21 as j and l get larger). Furthermore, measurements between epochs not adjacent in experimental time (i.e. epochs i and j where $i \neq j - 1$) are discarded yet contain useful information, despite perhaps being of poorer quality than measurements between adjacent epochs.

Instead of following these strategies we use a damped least-squares (DLS) inversion of relative traveltime perturbation measurements between all pairs of epochs that survive a minimum correlation threshold, to estimate the traveltime perturbation profile relative to a fixed reference epoch, wherein measurements with high variance are down-weighted. F. Brenguier *et al.* (2014) and C. Gómez-García *et al.* (2018) also use damped least-squares in a similar manner but down-weight measurements according to their correlation coefficient as opposed to using the full covariance matrix. The full covariance matrix is necessary to avoid under-estimating uncertainty in the inverted Δt profile. Arranging the relative mean Δt measurements, $\langle \Delta t_{ij} \rangle$ for all $\{i, j\}$, in column vector $\mathbf{d}$, with covariance matrix $Q_{\mathbf{d}}$, $\mathbf{d}$ is related to $\mathbf{m}$ through the linear equation

$$\mathbf{d} = G\mathbf{m} \tag{22}$$

where G represents the forward relationship from elements of $\mathbf{m}$ to the corresponding element of $\mathbf{d}$,

$$\langle \Delta t_{ij} \rangle = \langle \Delta t_{1j} \rangle - \langle \Delta t_{1i} \rangle . \tag{23}$$

This set of linear equations can be solved using a weighted least-squares inversion that is damped towards $\hat{\mathbf{m}}_{\mathrm{MR}}$ for stability:

$$\hat{\mathbf{m}}_{\mathrm{DLS}} = \Gamma^{-1}\left(G^T Q_{\mathbf{d}}^{-1}\mathbf{d} + \mu Q_{\hat{\mathbf{m}}_{\mathrm{MR}}}^{-1}\hat{\mathbf{m}}_{\mathrm{MR}}\right) \tag{24}$$

where

$$\Gamma^{-1} = \left(G^T Q_{\mathbf{d}}^{-1} G + \mu Q_{\hat{\mathbf{m}}_{\mathrm{MR}}}^{-1}\right)^{-1} \tag{25}$$

and μ is an adjustable parameter controlling the magnitude of damping of the solution towards $\hat{\mathbf{m}}_{\mathrm{MR}}$. A minimum correlation threshold was chosen whereby relative traveltime perturbation measurements from a correlation coefficient below the threshold are discarded, in order to ensure that $Q_{\mathbf{d}}$ is positive semidefinite. μ was chosen to minimize the root-mean-square error between the observed and predicted relative Δt measurements. Following this, using the standard method of R.C. Aster *et al.* (2019), the covariance matrix of $\hat{\mathbf{m}}_{\mathrm{DLS}}$ is calculated by

$$Q_{\hat{\mathbf{m}}_{\mathrm{DLS}}} = A\begin{bmatrix} Q_{\mathbf{d}} & 0 \\ 0 & Q_{\hat{\mathbf{m}}_{\mathrm{MR}}} \end{bmatrix} A^T \tag{26}$$

where

$$A = \begin{bmatrix} \Gamma^{-1} G^T Q_{\mathbf{d}}^{-1} \\ \Gamma^{-1}\mu Q_{\hat{\mathbf{m}}_{\mathrm{MR}}}^{-1} \end{bmatrix}^T . \tag{27}$$

In this way, all relative Δt measurements above the correlation coefficient threshold are used to minimize uncertainty in the inverted Δt profile, and measurements between epochs with a high correlation coefficient are preferentially weighted over those with a lower correlation coefficient in order to limit the impact of any errors arising from larger waveform changes during the experiment.

2.5 Energy partitioning inversion

The profile of Δt distributions relative to epoch 1 was found using the DLS method for a single coda window centred on time t_{w}, with distribution means as vector $\hat{\mathbf{m}}_{\mathrm{DLS}}(t_{\mathrm{w}})$ (eq. 24) and covariance matrix $Q_{\hat{\mathbf{m}}_{\mathrm{DLS}}}(t_{\mathrm{w}})$ (eq. 26). We denote the set of $\hat{\mathbf{m}}_{\mathrm{DLS}}(t_w)$ for all central window times t_{w} as $[\hat{\mathbf{m}}_{\mathrm{DLS}}(t_{\mathrm{w}})]$.

As described in Section 2.2.2, wave energy is partitioned between P and S waves according to the sensitivity kernel $q(t_{\mathrm{w}})$ (eq. 16), which is dependent on the P-to-S wave speed ratio α_j/β_j and the scattering mean free path traveltime $\tau_{p,j}$ at epoch j. This sensitivity kernel is used to decouple perturbations in P- and S-wave speed from traveltime perturbations throughout the coda (Fig. 1f). α_j/β_j was calculated from $\Delta\alpha_{1j}/\alpha_1$ and $\Delta\beta_{1j}/\beta_1$ by assuming a starting P-to-S wave speed ratio for the undeformed rock of $\alpha_1/\beta_1 = 1.52$, from measurements on Clashach sandstone by C. MacBeth (2004). We discuss the effect of this assumption in Section 4.4. We denote the set of profiles of P-wave speed perturbation, S-wave speed perturbation and the scattering mean free path traveltime, $\left\{\left[\Delta\alpha_{1j}/\alpha_1\right], \left[\Delta\beta_{1j}/\beta_1\right], \left[\tau_{p,j}\right]\right\}$ for all perturbed epochs j, as Θ. The nonlinear forward relationship in eq. (19) predicts Δt at coda time t_{w} and epoch j, given $\Delta\alpha_{1j}/\alpha_1$, $\Delta\beta_{1j}/\beta_1$ and $\tau_{\mathrm{p},j}$. We denote the predicted Δt profile at coda time t_{w} by $\hat{\mathbf{m}}_q(t_{\mathrm{w}})$, which is related to Θ through the forward relationship

$$\hat{\mathbf{m}}_q(t_{\mathrm{w}}) = g(t_{\mathrm{w}}, \Theta) \tag{28}$$

where g captures the nonlinear forward relationship from α_j/β_j and $\tau_{\mathrm{p},j}$ to $\Delta t_{1,j}(t_{\mathrm{w}})$ (eq. 19) for all perturbed epochs j.

The likelihood of the observed Δt profile at coda time t_{w}, $\hat{\mathbf{m}}_{\mathrm{DLS}}$, given Θ, was estimated by assuming that Δt follows a multivariate normal distribution with mean $\hat{\mathbf{m}}_{\mathrm{DLS}}(t_{\mathrm{w}})$ and covariance $Q_{\hat{\mathbf{m}}_{\mathrm{DLS}}}(t_{\mathrm{w}})$,

$$p\left(\hat{\mathbf{m}}_{\mathrm{DLS}}(t_{\mathrm{w}})\,|\Theta\right) = \frac{\exp\left(-\frac{1}{2}\epsilon^T Q_{\hat{\mathbf{m}}_{\mathrm{DLS}}}^{-1}\epsilon\right)}{(2\pi)^{N/2}\,|Q_{\hat{\mathbf{m}}_{\mathrm{DLS}}}|^{1/2}}, \tag{29}$$

where $\epsilon = \left(\hat{\mathbf{m}}_q - \hat{\mathbf{m}}_{\mathrm{DLS}}\right)$ and notation about the dependence of $\hat{\mathbf{m}}_q$, $\hat{\mathbf{m}}_{\mathrm{DLS}}$ and $Q_{\hat{\mathbf{m}}_{\mathrm{DLS}}}$ on t_w has been omitted for clarity, and N is the number of model parameters in Θ. The joint likelihood of the observed set of Δt profiles over all coda windows given Θ is therefore

$$p\left(\left[\hat{\mathbf{m}}_{\mathrm{DLS}}(t_{\mathrm{w}})\right]|\Theta\right) = \prod_{t_{\mathrm{w}}} p\left(\hat{\mathbf{m}}_{\mathrm{DLS}}(t_{\mathrm{w}})\,|\Theta\right). \tag{30}$$

To infer the posterior probability distribution of the profiles of P-wave speed perturbation, S-wave speed perturbation, and scattering mean free path traveltime, all represented by Θ, following observation of Δt profiles within different coda windows, represented by $[\hat{\mathbf{m}}_{\mathrm{DLS}}(t_{\mathrm{w}})]$, we used Bayes' rule,

$$p\left(\Theta|\left[\hat{\mathbf{m}}_{\mathrm{DLS}}(t_{\mathrm{w}})\right]\right) \propto p\left(\left[\hat{\mathbf{m}}_{\mathrm{DLS}}(t_{\mathrm{w}})\right]|\Theta\right) p(\Theta), \tag{31}$$

where $p\left(\Theta|\left[\hat{\mathbf{m}}_{\mathrm{DLS}}(t_{\mathrm{w}})\right]\right)$ is the *posterior* probability of Θ, representing our state of knowledge on Θ after assimilating information from the Δt profiles $[\hat{\mathbf{m}}_{\mathrm{DLS}}(t_{\mathrm{w}})]$, and $p(\Theta)$ is the *prior* probability of Θ, representing our state of knowledge of Θ before any measurements

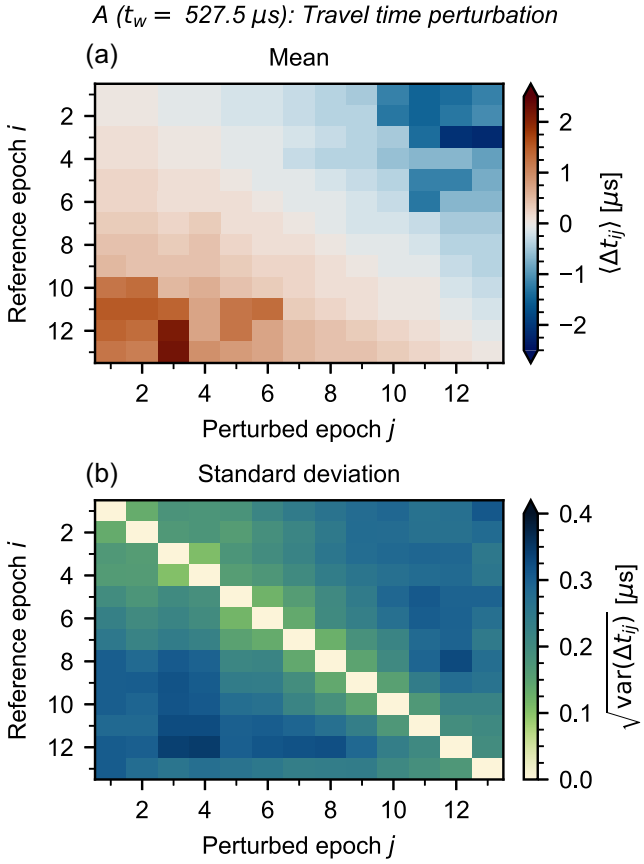

Figure 7. (a) The expectation $\langle \Delta t_{ij} \rangle$ and (b) the variance var (Δt_{ij}) of the distribution of traveltime perturbations of arrivals within the coda window centred at lapse time 527.5 μs between all epoch pairs $\{i, j\}$ in the dynamic experiment (A).

were taken. We used a largely uninformative prior–a uniform distribution with wide bounds on all parameters in Θ. We calculated the posterior distribution using the Metropolis–Hastings Markov chain Monte Carlo algorithm (K. Mosegaard & A. Tarantola 1995; A. Malinverno & S. Leaney 2000), whereby a chain of samples of Θ were generated with a target probability density of the posterior distribution. A sample Θ was first drawn from the prior distribution. Then, a new sample Θ' was drawn from a proposal distribution, and accepted into the model chain with probability

$$f\left(\Theta'|\Theta\right) = \min\left[\frac{p\left(\Theta'|\left[\hat{\mathbf{m}}_{\mathrm{DLS}}\left(t_{\mathrm{w}}\right)\right]\right)}{p\left(\Theta|\left[\hat{\mathbf{m}}_{\mathrm{DLS}}\left(t_{\mathrm{w}}\right)\right]\right)}, 1\right], \tag{32}$$

otherwise the same sample Θ was appended to the chain again (P.J. Green 1995). The proposal distribution was an adaptive isotropic multivariate normal distribution following M.J. Baker (2014), where the proposal distribution is iteratively updated towards the current best estimate of the posterior distribution—the current sample chain—and the covariance matrix was scaled to keep an average acceptance ratio of 0.234, as suggested by J.S. Rosenthal (2011), the update being increasingly damped at each iteration. 40 chains of 1000 000 samples are generated. The model chain stabilizes to the posterior distribution after a burn-in period. Then, the final ensemble of model samples was selected by decimating the sample chain to every 50th sample because successive models in the Markov chain are not independent, which can cause the estimated posterior distribution to be biased for a finite set of samples (C.J. Geyer & K.S. Chan 1994). The mean and 95 per cent credible interval of each parameter in Θ was taken from the ensemble of models.

3 RESULTS

Within a single coda window, the mean of the Δt distribution shows a general traveltime advance relative to the first epoch, which varies throughout the experiments and the variance of the Δt distribution increases when comparing epochs further apart in experimental time. For example, Fig. 7(a) shows that for a coda window during the dynamic experiment with central time 527.5 μs there is a mean traveltime advance increasing to ∼2 μs throughout the experiment, a trend that is broadly consistent for any reference epoch. The standard deviation of the Δt distribution within the window increases from ∼0.1–0.2 μs for measurements between epochs adjacent in experimental time, to ∼ 0.4 μs comparing epochs far apart in experimental time (Fig. 7b). (For an analysis of the full covariance matrix, see Appendix C.) Note also that var $(\Delta t_{ij}) \neq$ var (Δt_{ji}) due to the difference in the dominant mean square angular frequency

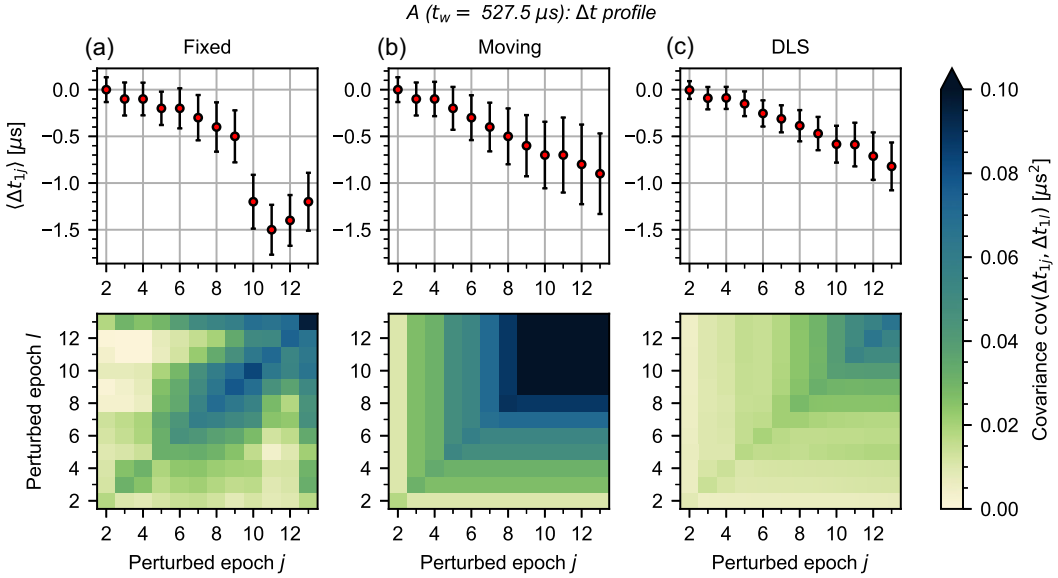

Figure 8. (Top) means (red dot) and standard deviations (error bars are ±1 standard deviation) of Δt distribution profiles estimated using (a) a fixed reference, (b) a moving reference and (c) DLS, and (bottom) the corresponding covariance matrix in a coda window centred at lapse time 527.5 μs during the dynamic experiment (A).

(eq. 7) between recordings at epoch i and j within the finite respective coda windows. The similarity of Δt trends using any reference epoch indicates that all relative measurements contain information about an underlying true Δt profile within the coda window, but the increase in variance for measurement pairs of epochs further apart in experimental time illustrates the need to down-weight these measurements during inversion.

The error in the Δt profile from DLS inversion is minimized as it uses as many relative Δt measurements as possible. (For an example of damping parameter selection, see Appendix D.) Within the example coda window, using a single reference epoch means that measurements further apart in experimental time were less reliable and often resulted in anomalous trends in the Δt profile such as jumps (Fig. 8a). The mean profiles using a moving reference and from DLS inversion were very similar (Figs 8b and c, respectively). However, error is accumulated throughout the moving reference profile and becomes significant at later epochs. The error for later epochs when using DLS inversion is less than half of that from using a moving reference.

The Δt profile shows an overall traveltime advance within coda windows at later times, but not linearly in proportion to the central time of the window. For earlier epochs, Δt is small throughout the coda during both the dynamic experiment (A, Fig. 9a) and quasi-static experiment (B, Fig. 9c). Δt generally advances with the central window time for later epochs, reaching a maximum of ∼1.5 μs in coda windows between ∼1000 and 1200 μs. Experiment B shows a slight traveltime delay during later epochs. Δt should approach zero as the traveltime approaches zero (eq. 13), however coda windows before ∼100 μs show an anomalous mean traveltime advance during experiment A that is greater than two standard deviations (Fig. 9b). During experiment B, the mean Δt shows the same behaviour for early epochs, however shows anomalously small mean Δt before ∼200 μs for later epochs. Note that the magnitude of the anomalies for experiment B are below one standard deviation (Fig. 9d). We discarded measurements using coda windows before 100 μs. The traveltime can be seen to advance with the central time of the window, with a steep gradient for earlier windows before stabilizing to a quasi-linear relationship between ∼300 and 400 μs. The nonlinear gradient in Δt with respect to t indicates that packets of energy arriving at different times travel through the medium from source to receiver with different path-averaged $\Delta v/v$, exhibiting a similar shape to that predicted by the energy partitioning model (Fig. 1e).

The sensitivity of Δt at a given epoch to $\Delta\alpha/\alpha$, $\Delta\beta/\beta$ and τ_p is given by an analytical sensitivity kernel (eq. 16). Following the procedure in Section 2.5, the analytical sensitivity kernel was inverted to provide estimates of $\Delta\alpha/\alpha$, $\Delta\beta/\beta$ and τ_p given the measured Δt profiles in all coda windows (Fig. 9). By visually inspecting the likelihood of each model chain, the likelihood appeared to become stationary after 10 000 iterations. These iterations were chosen to be the burn-in period and discarded. The width of the 95 per cent credible intervals for the inverted $\Delta\alpha/\alpha$ and $\Delta\beta/\beta$ profiles is on average 0.025 and 0.008 per cent (Figs 10a and b), respectively. This precision allows us to confidently resolve differences in the wave speed evolution between experiments A and B. $\Delta\alpha/\alpha$ followed an approximately linear increase following the onset of triaxial compression, however this trend slowed down after ∼1000 s during experiment B. Both experiments A and B reached peak $\Delta\alpha/\alpha$, of ∼0.3 and ∼0.2 per cent, respectively, at approximately 2000 s. Following this, $\Delta\alpha/\alpha$ plateaued during experiment A, and began to steadily decrease during experiment B after the acoustic emission feedback control began. $\Delta\beta/\beta$ shows an approximately linear increase with time—after ∼500 s during experiment B and ∼1000 s for experiment A. The peak $\Delta\beta/\beta$ shows the opposite relative relationship between the experiments compared to that of $\Delta\alpha/\alpha$, with experiment A

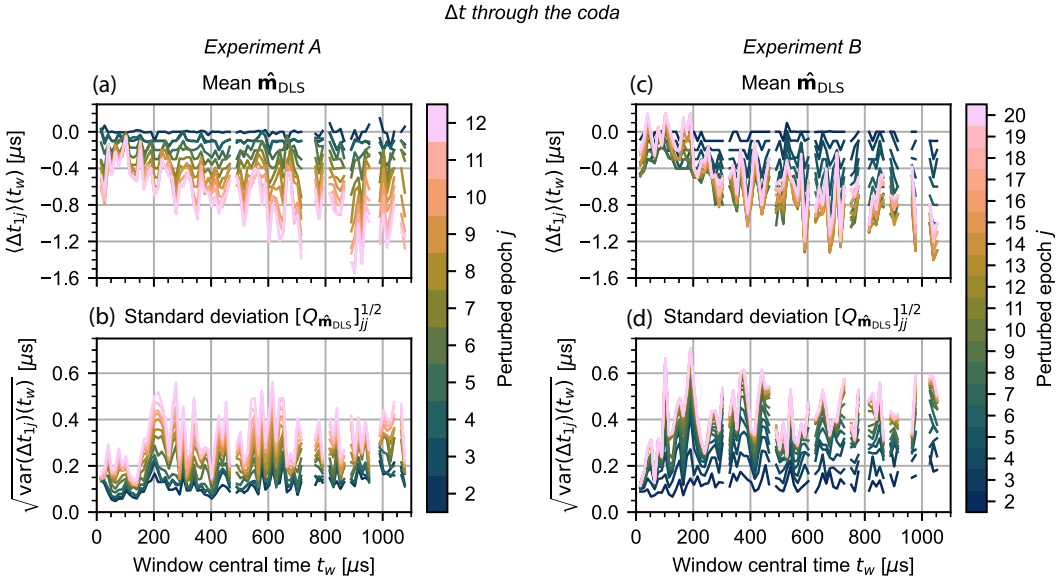

Figure 9. (a, c) Means $\langle \Delta t_{1j} \rangle$ and (b, d) standard deviations $\sqrt{\mathrm{var}\left(\Delta t_{1j}\right)}$ of the traveltime perturbations throughout the coda for each epoch j relative to epoch 1 during (a, b) the dynamic (A) and (c, d) quasi-static (B) experiments.

rising until failure to ∼0.04 per cent at ∼3000 s and experiment B rising to a peak of ∼0.07 per cent at ∼2400 s before slowly decreasing to ∼0.06 per cent during failure. The corresponding $\Delta\left(\alpha/\beta\right)/\left(\alpha/\beta\right)$ was similar to $\Delta\alpha/\alpha$, however decreased to near its original value (∼0.02 per cent) prior to failure during experiment B (Fig. 10d). During both experiments, τ_{p} began at ∼ 400 μs (Fig. 10c). During experiment A, it decreased to ∼300 μs until ∼1500 s before rising back to ∼400 μs just prior to failure. During experiment B, however, τ_{p} showed an approximately linear increase throughout the experiment to ∼800 μs. τ_{p} is better constrained for experiment A, with an average 95 per cent credible interval width ∼34 per cent that of experiment B.

4 DISCUSSION

4.1 Alternative coda wave interferometry methods

In order to provide a Δt estimate for every time sample within the waveform, T.D. Mikesell *et al.* (2015) used a dynamic time warping algorithm, which applies a nonlinear stretch to one waveform to match the point-by-point amplitude of another, and can be extended to consider local signal topology for robustness against noise (J.L. Li *et al.* 2024). However, different phases with the same traveltime at epoch i may not exhibit the same traveltime perturbation at epoch j, as they pass through different parts of the inhomogeneous velocity perturbation occurring between epochs i and j. Furthermore, a multiply-scattered arrival has a finite frequency bandwidth and hence cannot be represented by a single sample point in the coda so averaging traveltime perturbations within a finite-length time window is ultimately necessary.

Instead of the cross-correlation function being a function of a linear shift in time (i.e. the correlation between $u_i\left(t\right)$ and $u_j\left(t+\tau\right)$), C. Sens-Schönfelder & U. Wegler (2006) suggest the *trace stretching* method, whereby cross-correlation function is a function of a linear stretch in time, so that the stretching factor ϵ that maximizes the correlation between $u_i\left(t\right)$ and $u_j\left(t\left(1+\epsilon\right)\right)$ is $\left\langle \Delta v_{ij} \right\rangle / v_i$. Although this method is more robust to noise in the seismic data for long windows of equilibrated phases where $\Delta v_{ij}/v_i$ is time-invariant (C. Hadziioannou *et al.* 2009), we found that when using shorter coda windows required to characterize the variation of $\Delta v_{ij}/v_i$ with lapse time, there was little difference to the double wavelet method, particularly for windows centred at larger times and for small wave speed perturbations. This is because if the origin of the linear stretch is at $t=0$, then a transformation of the waveform within a small time window later in the coda is approximately a translation.

G. Poupinet *et al.* (1984) suggest the *moving window cross spectral* method, whereby the traveltime perturbation between two epochs within a window is measured by the gradient of a linear regression fit of the cross-correlation function phase spectrum, passing through zero, with the implicit assumption that waves of all frequencies experience the same traveltime perturbation. However, waves of different frequencies are sensitive to different scales of heterogeneities and take different scattered paths through the medium. Therefore, waves of different frequencies are not likely to experience exactly the same traveltime perturbation and the unwrapped phase spectrum is not necessarily linear. This is accounted for by the double wavelet method, which measures the *distribution* of Δt as opposed to a single value.

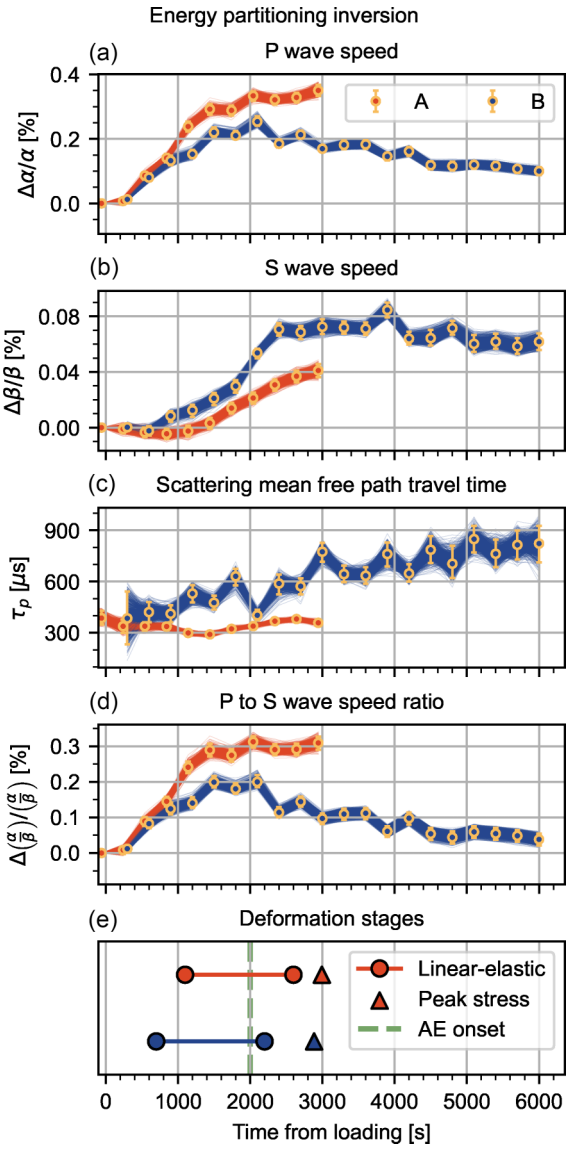

Figure 10. Samples from the model chain (lines) and the marginal mean (circles) and 95 per cent credible interval (error bars) of the (a) relative *P*-wave speed perturbation, (b) relative *S*-wave speed perturbation and (d) the subsequent perturbation of their ratio and (c) the scattering mean free path traveltime, during the dynamic (A, red) and quasi-static (B, blue) experiments. (e) The linear-elastic deformation regime begins after the loading onset and ends at the yield point, before reaching peak stress.

H. Douma & R. Snieder (2006) suggest applying a correction to eq. (6) to account for the decrease in the correlation coefficient due to the correlation of uncorrelated noise sources in addition to that of the desired signal. In effect, this decreases estimates of the variance of the Δt distribution. Using an estimate of noise amplitude from recordings of background noise preceding the triggered active shot, we found that this correction often overcorrects variance measurements, leading to negative variance estimates. This indicates that the noise is correlated between epochs or that the noise amplitude varies with lapse time. In either case, by not applying the correction we obtained an upper bound of variance measurements, meaning that uncertainties obtained in subsequent analyses are slightly overestimated, despite still being well-constrained.

To produce a Δt profile relative to a single reference epoch, the moving reference and DLS methods gave similar mean solutions however the variance of the DLS solution is much smaller. It is important to understand how we should interpret these results: In principle, a Δt profile that fits through twice the width of the uncertainty bars in Fig. 8 (± 2 standard deviations) and conforms to their associated covariances, is consistent with the relative Δt measurements and hence is potentially true for these samples. Therefore, one cannot infer from the moving reference solution that there is a statistically significant traveltime perturbation in the coda window shown in Fig. 8, because the constant value of zero Δt is a valid solution. However, this interpretation changes given the DLS solution due to the decreased variance. As the DLS covariance is smaller, the profile epochs are less correlated to each other and the solution is more informative.

Table 2. Linearized sensitivities of the energy partitioning equation to representative perturbations in model parameters, quantified by the L2 norm (sum over the coda, lapse time > 100 μs) of squared changes in the predicted traveltime perturbation. Only relative L2 norm magnitudes between parameters are meaningful. Ranges denote the interquartile range across inverted parameters in experiments A and B. Reported L2 norms correspond to representative perturbations of each parameter: changes in the relative *P*-wave speed perturbation $\Delta\alpha/\alpha$ of 0.2 per cent; changes in the relative *S*-wave speed perturbation $\Delta\beta/\beta$ of 0.04 per cent; changes in the scattering mean free path traveltime traveltime τ_p of 300 μs; a 1 per cent error in the source time t_0; a 1 per cent error in the reference *P*- to *S*-wave speed ratio α/β; and change in the proportion of *S*-wave energy q_0 by 1 per cent.

Variable	L2 norm [μs]
$\Delta\alpha/\alpha$	3.0–4.5
$\Delta\beta/\beta$	2.0–2.5
τ_p	2.0×10^{-1}–3.2×10^{-1}
t_0	1.4×10^{-3}–7.7×10^{-2}
α/β	2.2×10^{-2}–6.3×10^{-2}
q_0	1.0×10^{-2}–2.0×10^{-2}

4.2 Direct wave interferometry

By assuming that energy partitioning in the CWI window is in equilibrium, and hence the proportion of *P* to *S* waves is known given the *P*-to-*S* wave speed ratio, previous authors have used direct *P*-wave speed perturbation measurements to extract *S*-wave speed perturbations from CWI measurements (L. Griffiths *et al.* 2018; G. Sang *et al.* 2020; B. Zhong & J. Zhu 2022). However, it is advantageous to use energy partitioning inversion of the coda in ringdown mode as, unlike multiply-scattered *P* waves, the direct *P*-wave arrival is only sensitive to changes within a restricted volume around the fastest path, making it unrepresentative of the bulk volume (see Appendix A). Despite being of lower dominant frequency (Fig. 4b) and therefore a wider Fréchet kernel (K. Yomogida 1992; F.A. Dahlen *et al.* 2000; S.H. Hung *et al.* 2000), the restricted spatial sampling of the early coda produces significant observed deviations in behaviour between the early coda ($<$100 μs) and the late coda (Figs 9a and c). Furthermore, as the traveltime perturbation measurement for multiply-scattered waves is greater than for the direct wave, the proportional measurement error of the traveltime perturbation is smaller for multiply-scattered waves (J. Singh *et al.* 2019). The proportional measurement error is further reduced by using multiple measurements from different coda windows of multiply-scattered waves, as opposed to the single window used in direct wave interferometry.

4.3 Scattering model limitations

The energy partitioning inversion model assumes the coda wavefield is diffusive, that is, strongly scattered. However, coherent ballistic energy is typically present after the first arrival in real weakly scattering and heterogeneous systems, for example, primary reflections, free-surface and internal multiples and guided waves. Consequently, whilst the approach is well suited to high-frequency wavefields in strongly scattering media such as small sandstone cores, its effectiveness is reduced for field-scale systems where late ballistic arrivals are significant, for lower-frequency wavefields that are less sensitive to small-scale velocity fluctuations, or for weakly scattering homogeneous media that do not generate a long, diffuse coda.

4.4 Sensitivity to errors in fixed parameters

During energy partitioning inversion, we invert for three free parameters at each perturbed epoch—$\Delta\alpha/\alpha$, $\Delta\beta/\beta$ and τ_p—and fix the source time t_0, the reference *P*-to-*S* wave speed ratio $\alpha/\beta = 1.52$ (C. MacBeth 2004) and the proportion of *S* waves at zero lapse time $q_0 = 0$. As steps were taken to ensure accurate estimation of the source time (Section 2.1.2), the primary uncertainty in t_0 is the correction for traveltime through the pistons; the relative timing error decreases with increasing lapse time its influence is expected to be minor for late coda windows. Uncertainty in q_0 is also expected to be small as high-viscosity molasses and silicone grease were used to enhance transmission efficiency (Section 2.1.1), however some conversion to *S*-wave energy is unavoidable during propagation through the pistons (Fig. 2); this could be reduced by mounting sensors directly on the rock sample. We were unable to directly measure α/β for our samples in the absence of an *S*-wave transducer, making it the fixed parameter with the largest uncertainty; J. Singh *et al.* (2019) treat α/β as a free parameter.

To assess sensitivity, we derive the partial derivatives of the energy partitioning model (eq. B7) in Appendix E1 and compute the linearized response of Δt, quantified by the square root of the squared difference in Δt summed over the coda (L2 norm), to representative perturbations in the six parameters listed above (Table 2). Among the free parameters, the inversion is most sensitive to $\Delta\alpha/\alpha$ and least sensitive to τ_p. Perturbations in the free parameters produce L2 norm variations at least an order of magnitude larger than those associated with the fixed parameters, meaning the inversion is most sensitive to the free parameters, supporting our choice of parametrization.

4.5 Scattering mean free path traveltime

The scattering mean free path traveltime τ_p is the average timescale for an initial packet of *P*-wave energy to convert to an *S*-wave due to scattering. It increases with decreasing *P*-wave speed, decreasing probability of a *P* to *S* conversion and increasing average distance between scatterers. The initial response of τ_p to sample compression differed between experiments: decreasing in experiment A and increasing in experiment B. During both experiments, *P*-wave speed initially increases, so does not account for the difference in τ_p evolution. The probability of *P* to *S* conversion depends on the *P*-to-*S* wave speed ratio (L. Margerin *et al.* 2000), which shows the same behaviour as the *P*-wave speed evolution. Therefore, the τ_p evolution likely reflects changes in the average distance a between scatterers due to the movement, destruction or creation of scatterers or changes in the dominant frequency of the waveform. The sample in experiment A underwent more compaction before entering the quasi-elastic regime (Section 2.1.1), decreasing a, which explains why a decrease in τ_p is observed in experiment A and not experiment B. The subsequent increase in τ_p in both experiments may reflect the closure of heterogeneities such as pores which have a broad spatial distribution and the progressive localization of damage (M.D. Mangriotis *et al.* 2025).

For the theory of CWI to hold, the wavelength should be smaller than the scattering mean free path length (R. Snieder 2006). In this case, consecutive scattering events are independent and the wavefield does not become localized, that is, become trapped or confined to a small region (B.A. van Tiggelen 1999). The wave period of the applied bandpass is 1.0–2.5 μs, which is much smaller than the estimated scattering mean free path traveltime which is in the order of 10^2 μs. For *P* waves, however, the spatial wavelength corresponds to about half to one times the sample width. This indicates that multiples throughout the whole sample, and likely multiples through the pistons of the deformation rig, play a key role in the scattering that is observed in the extended coda. We acknowledge that some of the scattering will have occurred within the apparatus itself, implying that the observed wave speed evolution is an average over the sample and the apparatus. However, we expect relative changes in the wave speed of the sample to be larger than those of the apparatus because the stress sensitivities of elastic moduli are 2–3 orders of magnitude larger in Clashach sandstone (C. MacBeth 2004) than in non-compliant metals (D.S. Hughes & J.L. Kelly 1953; D.I. Crecraft 1967). Ideally, it would be advantageous to use higher-frequency transducers which provide a shorter wavelength.

4.6 Wave speed perturbation

Attenuation causes phase velocity dispersion to preserve causality (W.I. Futterman 1962). Changes in attenuation therefore perturb the traveltime between epochs, which is included in the mean and variance measurement of traveltime perturbations within each coda window. However, the traveltime perturbation due to changes in attenuation is expected to be an order of magnitude smaller than observed in this experiment (see Appendix E2); therefore, we can conclude that observed wave speed perturbations are dominated by changes in elastic constants and density. Attenuation can be included in the energy partitioning model by introducing two more free parameters—the attenuation coefficients of *P* and *S* waves, introducing an exponential dampening of *P*- and *S*-wave energy with time (R. Snieder & M. Deheuvels 2024). Differential attenuation of ultrasonic *P* and *S* waves is a well-known phenomenon in pressurized saturated sandstones (D.H. Johnston & M.N. Toksöz 1980), however we chose to assume a lossless medium to avoid introducing coupled parameters into the model and to keep the number of free parameters low, reducing computational cost.

The pressure vessel is X-ray transparent and deformation of the rock sample placed inside the pressure vessel was imaged *in situ* on beamline I12-JEEP at the Diamond Light Source using μCT imaging simultaneously with the repeated active ultrasonic pulse surveys, providing observations of the spatio-temporal evolution of the microstructure (A. Cartwright-Taylor *et al.* 2022; C. Elijas-Parra *et al.* 2025). X-ray tomographic scans scans show that there was a longer period of exploratory strain localization prior to microcrack damage localization along the eventual failure plane during the quasi-static experiment (B) compared to the dynamic experiment (A) and that microcracks were longer and more open in the latter with a broader shear zone and a greater degree of cataclasis and gouge throughout the sample (M.D. Mangriotis *et al.* 2025, figs 4 and 5). These microstructural differences in deformation between the experiments manifest differences in the bulk wave speed evolution as observed by CWI. Wave speed initially increases in response to local compaction, then decreases during strain softening stages, dominated by local dilation and local shear, respectively (A. Cartwright-Taylor *et al.* 2022). There are many mathematical and empirical models that link these microscale characteristics, such as crack density and crack geometry, to seismic wave speed (R.J. O'Connell & B. Budiansky 1974; J.G. Berryman 1980; P.A. Cilli & M. Chapman 2020). Crack density and geometry measurements from X-ray tomographic scans could be used to further inform rock physics models for wave speed evolution, in order to verify the wave speed evolution as obtained from CWI and energy partitioning inversion; however, this is beyond the scope of this work.

5 CONCLUSIONS

CWI has long been used to monitor subtle variations in the bulk seismic wave speed. However, conventional body-wave CWI cannot separate the relative contributions of *P* and *S* waves, which are sensitive to different material properties. In this work, we presented an energy partitioning inversion that uses a scattering-based model of modal energy partitioning to infer relative perturbations in *P*- and *S*-wave speeds, together with the scattering mean free path traveltime, from CWI measurements. The methodology is formulated

within a fully probabilistic framework: We demonstrated how to estimate the full covariance matrix of CWI measurements and how to obtain Bayesian posteriors for the separated *P*- and *S*-wave perturbations through energy partitioning inversion.

The approach was validated using repeated active ultrasonic surveys during dynamic and quasi-static rock deformation experiments. The results show that the combined CWI and energy partitioning framework can estimate wave speed perturbations with sufficient precision to distinguish statistically significant differences between deformation regimes.

ACKNOWLEDGMENTS

This work was supported by the UK's Natural Environment Research Council (NERC) through the CATFAIL project NE/R001693/1 Catastrophic failure: What controls precursory localization in rocks? (Principal Investigator I. G. Main), and the NERC Edinburgh Earth Ecology and Environment Doctoral Training Partnership grant NE/S007407/1. We acknowledge Diamond Light Source for time on beamline I12-JEEP under proposal MG22517 (Principal Investigator I. B. Butler) and the support of beamline scientist Dr Oxana Magdysuk and beamline technician Mr Robert Humphreys.

This work was initially conceptualized by M-DM and methodology was developed by J-AS. J-AS carried out formal analysis and visualization of results under the supervision of M-DM and AC. IGM obtained funding for the CATFAIL project and data was collected by AC-T and IBB and curated by XL. XL provided regular feedback during the analysis stage. J-AS produced the initial manuscript draft, which was refined by all authours. We thank Dr Xuebin Zhao for his advice on adaptive Markov-chain Monte Carlo methods. We also thank two anonymous reviewers for their constructive comments, which greatly improved the manuscript.

DATA AVAILABILITY

The raw acoustic waveforms and raw mechanical data used in this study are available at the NERC EDS National Geoscience Data Centre repository under accession code: https://webapps.bgs.ac.uk/services/ngdc/accessions/index.html#item173296, with direct access to the data set available at the NERC STFC Centre for Environmental Data Analysis third party holdings: https://data.ceda.ac.uk/ngdc/NE_R001693_1. Experiments A and B in this study are samples CL04 and CL10, respectively. These data are available under Open Government Licence (OGL). When using the data set held in the repository, please cite A. Cartwright-Taylor *et al.* (2022).

REFERENCES

Aki, K., 1969. Analysis of the seismic coda of local earthquakes as scattered waves, *J. geophys. Res.,* **74**(2), 615–631.
Allen, R.V., 1978. Automatic earthquake recognition and timing from single traces, *Bull. seism. Soc. Am.,* **68**(5), 1521–1532.
Arnold, R. & Curtis, A., 2018. Interrogation theory, *Geophys. J. Int.,* **214**(3), 1830–1846.
Arts, R.J., Elsayed, R., van der Meer, L., Eiken, O., Ostmo, S., Chadwick, A., Kirby, G. & Zinszner, B., 2002. Estimation of the mass of injected CO2 at Sleipner using time-lapse seismic data. *64th EAGE Conference and Exhibition,* European Association of Geoscientists and Engineers.
Aster, R.C., Borchers, B. & Thurber, C.H., 2019. *Parameter Estimation and Inverse Problems,* 3rd edn, Elsevier
Baker, M.J., 2014. Adaptive Markov Chain Monte Carlo sampling and estimation in Mata, *The Stata Journal: Promoting Communications on Statistics and Stata,* **14**(3), 623–661.
Berryman, J.G., 1980. Long-wavelength propagation in composite elastic media II. Ellipsoidal inclusions, *J. Acoust. Soc. Am.,* **68**(6), 1820–1831.
Birch, F., 1960. The velocity of compressional waves in rocks to 10 kilobars: 1., *J. geophys. Res.,* **65,** 1083–1102.
Boschetti, F., Dentith, M.D. & List, R.D., 1996. A fractal-based algorithm for detecting first arrivals on seismic traces, *Geophysics,* **61,** 1095–1102.
Bourne, S.J., Oates, S.J., van Elk, J. & Doornhof, D., 2014. A seismological model for earthquakes induced by fluid extraction from a subsurface reservoir, *J. Geophys. Res.: Solid Earth,* **119,** 8991–9015.
Brenguier, F., Shapiro, N.M., Campillo, M., Ferrazzini, V., Duputel, Z., Coutant, O. & Nercessian, A., 2008. Towards forecasting volcanic eruptions using seismic noise, *Nat. Geosci.,* **1,** 126–130.
Brenguier, F., Campillo, M., Takeda, T., Aoki, Y., Shapiro, N.M., Briand, X., Emoto, K. & Miyake, H., 2014. Mapping pressurized volcanic fluids from induced crustal seismic velocity drops, *Science,* **345,** 80–82.
Bucci, O.M. & Franceschetti, G., 1989. On the degrees of freedom of scattered fields, *IEEE Trans. Antennas Propag.,* **37,** 918–926.
Bunks, C., Saleck, F.M., Zaleski, S. & Chavent, G., 1995. Multiscale seismic waveform inversion, *Geophysics,* **60,** 1457–1473 .
Butler, I., Fusseis, F., Cartwright-Taylor, A. & Flynn, M., 2020. Mjölnir: a miniature triaxial rock deformation apparatus for 4D synchrotron X-ray microtomography, *J. Synchrotron Radiat.,* **27,** 1681–1687.
Cartwright-Taylor, A. *et al.*, 2022. Seismic events miss important kinematically governed grain scale mechanisms during shear failure of porous rock, *Nat. Commun.,* **13,** 6169 .
Cilli, P.A. & Chapman, M., 2020. The power-law relation between inclusion aspect ratio and porosity: implications for electrical and elastic modeling, *J. Geophys. Res.: Solid Earth,* **125,** e2019JB019187.
Cooley, J.W. & Tukey, J.W., 1965. An algorithm for the machine calculation of complex Fourier series, *Math. Comput.,* **19**(90), 297–301.
Crecraft, D.I., 1967. The measurement of applied and residual stresses in metals using ultrasonic waves, *J. Sound Vib.,* **5**(1), 173–192.
Dahlen, F.A., Hung, S.H. & Nolet, G., 2000. Fréchet kernels for finite-frequency traveltimes—I. Theory, *Geophys. J. Int.,* **141,** 157–174.
de Ridder, S.A.L. & Biondi, B.L., 2013. Daily reservoir-scale subsurface monitoring using ambient seismic noise, *Geophys. Res. Lett.,* **40,** 2969–2974.
Douma, H. & Snieder, R., 2006. Correcting for bias due to noise in coda wave interferometry, *Geophys. J. Int.,* **164,** 99–108.
Dresen, G., Kwiatek, G., Goebel, T. & Ben-Zion, Y., 2020. Seismic and aseismic preparatory processes before large stick–slip failure, *Pure appl. Geophys.,* **177,** 5741–5760.
Earle, P.S. & Shearer, P.M., 1994. Characterization of global seismograms using an automatic-picking algorithm, *Bull. seism. Soc. Am.,* **84,** 366–376.

Elijas-Parra, C., Cartwright-Taylor, A., Main, I.G., Ursu, R.E., Butler, I.B. & Fusseis, F., 2025. Controls on shear band orientation in deforming porous rocks: insights from improved microcrack segmentation method, *J. Struct. Geol.,* **196,** 105 404.
Ervin, C.P., McGinnis, L.D., Otis, R.M. & Hall, M.L., 1983. Automated analysis of marine refraction data: a computer algorithm, *Geophysics,* **48,** 582–589.
Evans, J.R. & Allen, S.S., 1983. A teleseism-specific detection algorithm for single short-period traces, *Bull. seism. Soc. Am.,* **73,** 1173–1186.
Foulger, G.R., Wilson, M.P., Gluyas, J.G., Julian, B.R. & Davies, R.J., 2018. Global review of human-induced earthquakes, *Earth Sci. Rev.,* **178,** 438–514.
Futterman, W.I., 1962. Dispersive body waves, *J. geophys. Res.,* **67**(13), 5279–5291 .
Gassenmeier, M., Sens-Schönfelder, C., Delatre, M. & Korn, M., 2014. Monitoring of environmental influences on seismic velocity at the geological storage site for CO2 in Ketzin (Germany) with ambient seismic noise, *Geophys. J. Int.,* **200,** 524–533.
Geyer, C.J. & Chan, K.S., 1994. Discussion of the paper by Tierney, *Ann. Stat.,* **22,** 1747–1758.
Gómez-García, C., Brenguier, F., Boué, P., Shapiro, N.M., Droznin, D.V., Droznina, S.Y., Senyukov, S.L. & Gordeev, E.I., 2018. Retrieving robust noise-based seismic velocity changes from sparse data sets: synthetic tests and application to Klyuchevskoy volcanic group (Kamchatka), *Geophys. J. Int.,* **214,** 1218–1236 .
Green, P.J., 1995. Reversible jump Markov chain Monte Carlo computation and Bayesian model determination, *Biometrika,* **82,** 711–732.
Griffiths, L., Lengliné, O., Heap, M.J., Baud, P. & Schmittbuhl, J., 2018. Thermal cracking in westerly granite monitored using direct wave velocity, coda wave interferometry, and acoustic emissions, *J. Geophys. Res.: Solid Earth,* **123,** 2246–2261.
Hadziioannou, C., Larose, E., Coutant, O., Roux, P. & Campillo, M., 2009. Stability of monitoring weak changes in multiply scattering media with ambient noise correlation: Laboratory experiments, *J. Acoust. Soc. Am.,* **125,** 3688–3695.
Hatherly, P.J., 1982. A computer method for determining seismic first arrival times, *Geophysics,* **47,** 1431–1436.
Hughes, D.S. & Kelly, J.L., 1953. Second-order elastic deformation of solids, *Phys. Rev.,* **92**(5), 1145–1149.
Hung, S.H., Dahlen, F.A. & Nolet, G., 2000. Fréchet kernels for finite-frequency traveltimes - II. Examples, *Geophys. J. Int.,* **141,** 175–203.
Johnston, D.H., 2013. *Practical Applications of Time-lapse Seismic Data,* 1st edn, Society of Exploration Geophysicists.
Johnston, D.H. & Toksöz, M.N., 1980. Ultrasonic P and S wave attenuation in dry and saturated rocks under pressure, *J. Geophys. Res.: Solid Earth,* **85,** 925–936.
Landau, H.J., 1967. Necessary density conditions for sampling and interpolation of certain entire functions, *Acta Math.,* **117,** 37–52.
Landrø, M. & Stammeijer, J., 2004. Quantitative estimation of compaction and velocity changes using 4D impedance and traveltime changes, *Geophysics,* **69,** 949–957 .
Larose, E. & Hall, S., 2009. Monitoring stress related velocity variation in concrete with a 2×10^{-5} relative resolution using diffuse ultrasound, *J Acoust. Soc. Am.,* **125,** 1853–1856.
Lecocq, T., Longuevergne, L., Pedersen, H.A., Brenguier, F. & Stammler, K., 2017. Monitoring ground water storage at mesoscale using seismic noise: 30 years of continuous observation and thermo-elastic and hydrological modeling, *Sci. Rep.,* **7,** 14 241.
Li, J.L., Huang, W.L. & Zhang, R.X., 2024. Seismic data extrapolation based on multi-scale dynamic time warping, *Petrol. Sci.,* **21,** 3981–4000.
Lobkis, O.I. & Weaver, R.L., 2001. On the emergence of the Green's function in the correlations of a diffuse field, *J. Acoust. Soc. Am.,* **110,** 3011–3017.
Lockner, D.A., Byerlee, J.D., Kuksenko, V., Ponomarev, A. & Sidorin, A., 1991. Quasi-static fault growth and shear fracture energy in granite, *Nature,* **350,** 39–42.
Lockner, D.A., Byerlee, J.D., Kuksenko, V., Ponomarev, A. & Sidorin, A., 1992. Chapter 1 Observations of quasistatic fault growth from acoustic emissions, *Fault Mechanics and Transport Properties of Rocks, Vol. 51 of International Geophysics,* pp. 3–31, Academic Press.
MacBeth, C., 2004. A classification for the pressure-sensitivity properties of a sandstone rock frame, *Geophysics,* **69,** 497–510.
Malinverno, A. & Leaney, S., 2000. A Monte Carlo method to quantify uncertainty in the inversion of zero-offset VSP data. *2000 SEG Annual Meeting, Calgary, Alberta*. Society of Exploration Geophysicists.
Mangriotis, M.D., Cartwright-Taylor, A., Main, I.G., Curtis, A., Bell, A.F., Butler, I.B. & Fusseis, F., 2025. Loading of a porous rock with constant microseismic event rate suppresses seismicity and promotes subcritical failure, *Sci. Rep.,* **15,** 19 351.
Margerin, L., Campillo, M. & van Tiggelen, B., 2000. Monte Carlo simulation of multiple scattering of elastic waves, *J. Geophys. Res.: Solid Earth,* **105,** 7873–7892.
McLaskey, G.C. & Glaser, S.D., 2012. Acoustic emission sensor calibration for absolute source measurements, *J. Nondestruct. Eval.,* **31,** 157–168.
Meier, U., Shapiro, N.M. & Brenguier, F., 2010. Detecting seasonal variations in seismic velocities within Los Angeles basin from correlations of ambient seismic noise, *Geophys. J. Int.,* **181,** 985–996 .
Meredith, P.G. & Atkinson, B.K., 1983. Stress corrosion and acoustic emission during tensile crack propagation in Whin Sill dolerite and other basic rocks, *Geophys. J. Int.,* **75,** 1–21.
Mikesell, T.D., Malcolm, A.E., Yang, D. & Haney, M.M., 2015. A comparison of methods to estimate seismic phase delays: numerical examples for coda wave interferometry, *Geophys. J. Int.,* **202,** 347–360.
Molyneux, J.B. & Schmitt, D.R., 1999. First-break timing: arrival onset times by direct correlation, *Geophysics,* **64,** 1492–1501.
Mordret, A., Mikesell, T.D., Harig, C., Lipovsky, B.P. & Prieto, G.A., 2016. Monitoring southwest Greenland's ice sheet melt with ambient seismic noise, *Sci. Adv.,* **2,** e1501538.
Mosegaard, K. & Tarantola, A., 1995. Monte Carlo sampling of solutions to inverse problems, *J. Geophys. Res.: Solid Earth,* **100,** 12 431–12 447.
Obermann, A., Kraft, T., Larose, E. & Wiemer, S., 2015. Potential of ambient seismic noise techniques to monitor the St. Gallen geothermal site (Switzerland), *J. Geophys. Res.: Solid Earth,* **120,** 4301–4316.
O'Connell, R.J. & Budiansky, B., 1974. Seismic velocities in dry and saturated cracked solids, *J. geophys. Res.,* **79,** 5412–5426.
Olivier, G., Brenguier, F., Campillo, M., Roux, P., Shapiro, N.M. & Lynch, R., 2015. Investigation of coseismic and postseismic processes using in situ measurements of seismic velocity variations in an underground mine, *Geophys. Res. Lett.,* **42,** 9261–9269.
Peraldi, R. & Clement, A., 1972. Digital processing of refraction data study of first arrivals, *Geophys. Prospect.,* **20,** 529–548.
Picozzi, M. *et al.*, 2011. Interferometric analysis of strong ground motion for structural health monitoring: the example of the L'Aquila, Italy, seismic sequence of 2009, *Bull. seism. Soc. Am.,* **101,** 635–651.
Planès, T. & Larose, E., 2013. A review of ultrasonic Coda Wave Interferometry in concrete, *Cement Concrete Res.,* **53,** 248–255.
Planès, T., Mooney, M.A., Rittgers, J.B.R., Parekh, M.L., Behm, M. & Snieder, R., 2016. Time-lapse monitoring of internal erosion in earthen dams and levees using ambient seismic noise, *Géotechnique,* **66,** 301–312.
Poupinet, G., Ellsworth, W.L. & Frechet, J., 1984. Monitoring velocity variations in the crust using earthquake doublets: an application to the Calaveras Fault, California, *J. Geophys. Res.: Solid Earth,* **89,** 5719–5731.

Rosenthal, J.S., 2011. Optimal proposal distributions and adaptive MCMC, *Handbook of Markov Chain Monte Carlo,* 1st edn, pp. 93–111, Chapman and Hall/CRC,.
Sabra, K.G., Conti, S., Roux, P. & Kuperman, W.A., 2007. Passive in vivo elastography from skeletal muscle noise, *Appl. Phys. Lett.,* **90,** 194 101.
Sammonds, P.R., Meredith, P.G. & Main, I.G., 1992. Role of pore fluids in the generation of seismic precursors to shear fracture, *Nature,* **359,** 228–230.
Sang, G., Liu, S. & Elsworth, D., 2020. Quantifying fatigue-damage and failure-precursors using ultrasonic coda wave interferometry, *Int. J. Rock Mech. Min. Sci.,* **131,** 104 366.
Sens-Schönfelder, C. & Wegler, U., 2006. Passive image interferometry and seasonal variations of seismic velocities at Merapi Volcano, Indonesia, *Geophys. Res. Lett.,* **33,** L21302.
Singh, J., Curtis, A., Zhao, Y., Cartwright-Taylor, A. & Main, I., 2019. Coda wave interferometry for accurate simultaneous monitoring of velocity and acoustic source locations in experimental rock physics, *J. Geophys. Res.: Solid Earth,* **124,** 5629–5655.
Smith, J.A. *et al.*, 2021. Seismic characterisation of rock failure in a dynamic loading experiment. *14th Euroconference on Rock Physics and Rock Mechanics.*
Snieder, R., 1986. 3-D linearized scattering of surface waves and a formalism for surface wave holography, *Geophys. J. Int.,* **84,** 581–605.
Snieder, R., 2002. Coda wave interferometry and the equilibration of energy in elastic media, *Phys. Rev. E,* **66,** 046 615.
Snieder, R., 2004. Extracting the Green's function from the correlation of coda waves: a derivation based on stationary phase, *Phys. Rev. E,* **69,** 046 610.
Snieder, R., 2006. The theory of coda wave interferometry, *Pure appl. Geophys.,* **163,** 455–473.
Snieder, R. & Deheuvels, M., 2024. Energy partitioning among compressional and shear waves in three-dimensional attenuating elastic media, *J. Acoust. Soc. Am.,* **155,** 3336–3344.
Snieder, R., Grêt, A., Douma, H. & Scales, J., 2002. Coda wave interferometry for estimating nonlinear behavior in seismic velocity, *Science,* **295,** 2253–2255.
St-Onge, A., 2011. Akaike information criterion applied to detecting first arrival times on microseismic data. *SEG Technical Program Expanded Abstracts 2011,* pp. 1658 -1662, Society of Exploration Geophysicists.
Stähler, S.C., Sens-Schönfelder, C. & Niederleithinger, E., 2011. Monitoring stress changes in a concrete bridge with coda wave interferometry, *J. Acoust. Soc. Am.,* **129,** 1945–1952.
Swindell, S.W. & Snell, N.S., 1977. Station processor automatic signal detection system, phase I: final report, station processor software development, Final report no. alex (01)-fr-77-01, Texas Instruments.
Tant, K.M.M., Galetti, E., Mulholland, A.J., Curtis, A. & Gachagan, A., 2018. A transdimensional Bayesian approach to ultrasonic travel-time tomography for non-destructive testing, *Inverse Problems,* **34**(9), 095 002.
Tant, K.M.M., Galetti, E., Mulholland, A.J., Curtis, A. & Gachagan, A., 2020. Effective grain orientation mapping of complex and locally anisotropic media for improved imaging in ultrasonic non-destructive testing, *Inverse Problems Sci. Eng.,* **28**(12), 1694–1718.
Terada, M., Yanagidani, T. & Ehara, S., 1984. A.E. rate controlled compression tests of rocks, *3rd Conference on Acoustic Emission / Microseismic Activity in Geological Structures and Materials,* pp. 159–171, Trans-Tech Publications.
Tsai, V.C., 2011. Understanding the amplitudes of noise correlation measurements, *J. geophys. Res.,* **116,** B09311.
van Tiggelen, B.A., 1999. Localization of waves, *Diffuse Waves in Complex Media,* 1st edn, pp. 1–60, Springer-Verlag, Berlin.
Vlastos, S., Liu, E., Main, I.G., Schoenberg, M., Narteau, C., Li, X.Y. & Maillot, B., 2006. Dual simulations of fluid flow and seismic wave propagation in a fractured network: effects of pore pressure on seismic signature, *Geophys. J. Int.,* **166,** 825–838.
Vlastos, S., Liu, E., Main, I.G. & Narteau, C., 2007. Numerical simulation of wave propagation in 2-D fractured media: scattering attenuation at different stages of the growth of a fracture population, *Geophys. J. Int.,* **171,** 865–880.
Walters, R.J., Zoback, M.D., Baker, J.W. & Beroza, G.C., 2015. Characterizing and responding to seismic risk associated with earthquakes potentially triggered by fluid disposal and hydraulic fracturing, *Seismol. Res. Lett.,* **86,** 1110–1118.
Weaver, R.L. & Lobkis, O.I., 2001. Ultrasonics without a Source: Thermal Fluctuation Correlations at MHz Frequencies, *Phys. Rev. Lett.,* **87,** 134 301.
Wegler, U. & Sens-Schönfelder, C., 2007. Fault zone monitoring with passive image interferometry, *Geophys. J. Int.,* **168,** 1029–1033.
Yomogida, K., 1992. Fresnel zone inversion for lateral heterogeneities in the earth, *Pure appl. Geophys.,* **138,** 391–406.
Zhong, B. & Zhu, J., 2022. Applications of stretching technique and time window effects on ultrasonic velocity monitoring in concrete, *Appl. Sci.,* **12,** 7130.
Zorgani, A., Souchon, R., Dinh, A.H., Chapelon, J.Y., Ménager, J.M., Lounis, S., Rouvière, O. & Catheline, S., 2015. Brain palpation from physiological vibrations using MRI, *Proc. Natl. Acad. Sci. USA,* **112,** 12 917–12 921.

APPENDIX A: FIRST-BREAK PICKING AND DIRECT WAVE INTERFEROMETRY

In the main text, we use interferometry in late coda windows to determine relative bulk wave speed perturbations. J.A. Smith *et al.* (2021) compared the relative wave speed perturbation inferred from both first-break picks and interferometry with a coda window over the first arrival of wave energy using the same active data during the dynamic experiment.

The absolute traveltime along the fastest path through the medium can be measured from the lapse time of the first break of wave energy. Assuming a rectilinear ray path from source to receiver, this can be converted to absolute velocity, corresponding to *P*-wave velocity assuming the wave energy spent the entire path in a *P*-wave state. J.A. Smith *et al.* (2021) used four different first-break picking algorithms (with frequency band 0.4–1.0 MHz): conventional short-term-average/long-term-average (STA/LTA; R.V. Allen 1978), recursive STA/LTA (J.R. Evans & S.S. Allen 1983), the Z-detector (S.W. Swindell & N.S. Snell 1977) and Akaike information criterion detector (AIC) (A. St-Onge 2011). Assuming an initial wave speed of 3920 ms^{-1} (C. MacBeth 2004), relative wave speed perturbations reach a maximum of ∼10 per cent with a range of ∼5 per cent between algorithms with non-erroneous measurements (Fig. A1). The principle of source–receiver reciprocity implies the results should be the same whether using the bottom or top sensor as the source, however these results also differed on the order of ∼5 per cent. This demonstrates the large relative error of first-break picking methods for very small traveltime perturbations.

Table A1. Summary of variables in energy partitioning equation.

Δt	Traveltime perturbation for phase at lapse time t
q	Proportion of S waves at lapse time t ($q_0 \equiv q\|_{t=0}$)
α_Δ	Relative change in P-wave speed with respect to reference state (denoted $\Delta\alpha/\alpha$ in main text)
β_Δ	Relative change in S-wave speed with respect to reference state (denoted $\Delta\beta/\beta$ in main text)
κ	P-to-S wave speed ratio (denoted α/β in main text), κ_0 in reference state
τ_p	Scattering mean free path traveltime

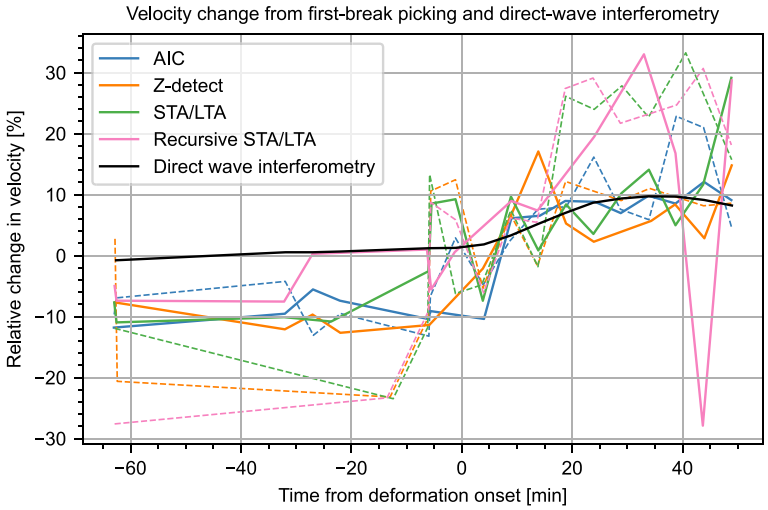

Figure A1. Estimated relative velocity change during the dynamic experiment from cross-correlation of an lapse time window at the wave train onset (direct wave interferometry) and first-break picks (AIC, Z-detect, STA/LTA and recursive STA/LTA algorithms) assuming a rectilinear ray path from source to receiver and an initial velocity of 3920 ms^{-1} with the bottom (dashed line) and top (solid line) transducers as sources.

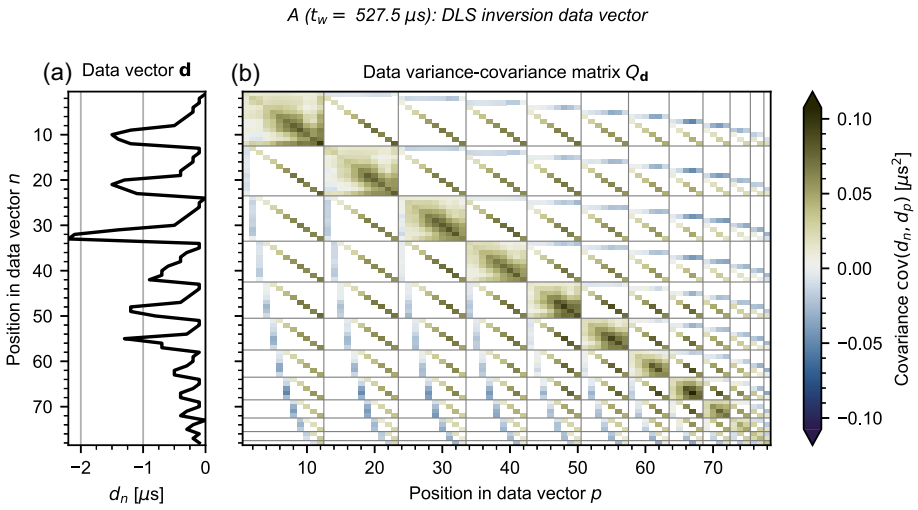

Figure A2. (a) The data and (b) covariance matrix of relative traveltime perturbation measurements to invert for the traveltime perturbation profile, **d** and $Q_\mathbf{d}$ in eq. (24), respectively, built from measurements in Fig. 7).

J.A. Smith *et al.* (2021) showed that using interferometry with a moving reference in a 150 μs window at the onset of wave energy (direct wave interferometry, DWI) yields a smoother profile (Fig. A1). The magnitude of relative wave speed perturbations is similar to first-break picks, however measurements are accurate enough to show key features of the wave speed profile, for example, steadily increasing wave speed following deformation onset followed by a decrease in wave speed prior to failure.

Relative wave speed perturbations from first-break picks and DWI are an order of magnitude greater than those measured from CWI in the main text. This is because CWI measures changes in the bulk medium as opposed to changes along the fastest path, which is clearly unrepresentative of the bulk medium in this case. This indicates that velocity changes are spatially localized, which is supported by the spatial localization of damage observed by M.D. Mangriotis *et al.* (2025) using X-ray tomography.

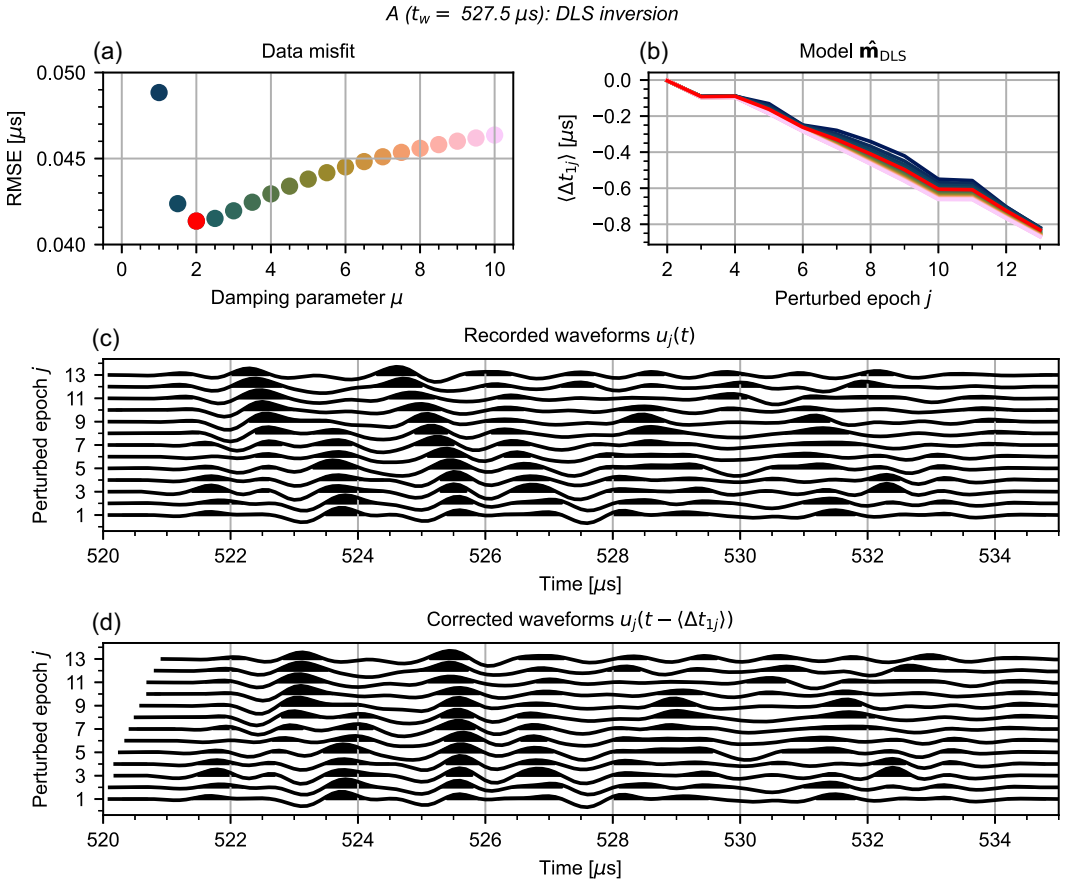

Figure A3. (a) Selection of the optimal damping parameter to minimize the root-mean-square error (RMSE) of the observed to the predicted relative Δt measurements of (b) the DLS solution for the Δt profile. Colours in panel (b) correspond to damping parameters shown in panel (a). Red shows the DLS solution with the lowest RMSE value. (c) Arrivals on the uncorrected waveforms show perturbations in traveltime between each epoch, (d) which were used to validate the inverted model by checking whether they have been aligned after correcting for the perturbation.

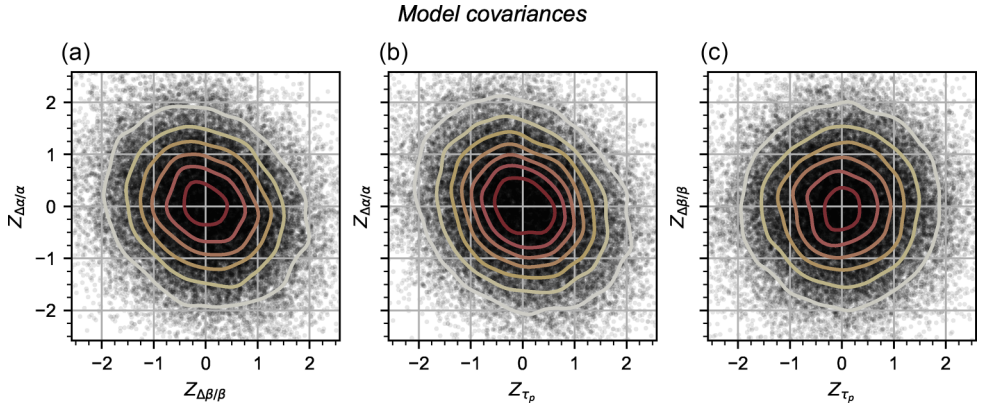

Figure A4. Trade-off between standardized model parameters across the model chain: *P*-wave speed perturbation $Z_{\Delta\alpha/\alpha}$, *S*-wave speed perturbation $Z_{\Delta\beta/\beta}$ and traveltime of the scattering mean free path Z_{τ_p}. All model samples are plotted with a kernel density estimate overlaid.

APPENDIX B: *P* AND *S*-WAVE ENERGY PARTITIONING EQUATIONS

R. Snieder (2002) introduces a set of simultaneous differential equations for the rate of change of the number of packets of *P*-wave energy N_P and *S*-wave energy N_S in the wavefield (eqs 14 and 15, respectively). Here, we show how to derive an analytical solution to the variation of the relative proportion of packets of *P*- and *S*-wave energy with lapse time, assuming the medium is non-attenuative and that all the packets of energy begin in the *P*-wave state, that is, the source is purely compressional.

Let l_P be the scattering mean free path, defined as $a/2p_{PS}$, where p_{PS} is the probability that a packet of *P*-wave energy converts to a packet of *S*-wave energy during a single scattering event, and vice versa for p_{SP} and a is the average distance between scattering events.

The traveltime of one scattering mean free path is therefore

$$\tau_{\mathrm{p}} = \frac{l_{\mathrm{p}}}{\alpha} = \frac{a}{2p_{\mathrm{PS}}\alpha}, \tag{B1}$$

where α is the P-wave speed. τ_{p} is used to define the normalized time $t' = t/\tau_{\mathrm{p}}$. Furthermore, from the ratio of the scattering cross-sections from P to S scattering and S to P scattering, the ratio $p_{\mathrm{SP}}/p_{\mathrm{PS}}$ in a non-attenuative medium is given by L. Margerin *et al.* (2000) as

$$\frac{p_{\mathrm{SP}}}{p_{\mathrm{PS}}} = \left(\frac{\beta}{\alpha}\right)^2 \tag{B2}$$

where β is the S-wave speed. Letting $\dot{N}'_{\mathrm{S}} = \mathrm{d}N_{\mathrm{S}}/\mathrm{d}t'$ and combining eqs (15), (B1) and (B2) gives

$$\dot{N}'_{\mathrm{S}} = \tau_{\mathrm{p}}\dot{N}_{\mathrm{S}} = N_{\mathrm{P}} - \frac{1}{2}\left(\frac{\beta}{\alpha}\right)^3 N_{\mathrm{S}}\,. \tag{B3}$$

Let q be the relative proportion of S-wave packets,

$$q = \frac{N_{\mathrm{S}}}{N_{\mathrm{P}} + N_{\mathrm{S}}}\,. \tag{B4}$$

If no wave packets are lost, that is, $(N_{\mathrm{P}} + N_{\mathrm{S}})$ is constant, using eqs (B3) and (B4), $\dot{q}' = \mathrm{d}q/\mathrm{d}t'$ is

$$\dot{q}' = \frac{\dot{N}'_{\mathrm{S}}}{N_{\mathrm{P}} + N_{\mathrm{S}}} = 1 - \gamma q \tag{B5}$$

where

$$\gamma = \frac{1}{2}\left(\frac{\beta}{\alpha}\right)^3 + 1\,. \tag{B6}$$

Letting q at $t' = 0$ be q_0, the solution to eq. (B5) is:

$$q = \frac{1}{\gamma}\left(1 - (1 - \gamma q_0)e^{-\gamma t'}\right)\,. \tag{B7}$$

Assuming that the packets of energy all begin in the P-wave state, that is, $q_0 = 0$, eq. (B7) becomes:

$$q = \frac{1}{\gamma}\left(1 - e^{-\gamma t'}\right)\,. \tag{B8}$$

APPENDIX C: ANALYSIS OF THE COVARIANCE MATRIX

Δt measurements are not independent if the measurement pairs share a common epoch, and their covariance is of the same order of magnitude as the variance of a single measurement. After flattening the upper triangle of the matrix of Δt measurements between all measurement pairs (Fig. 7a) into a vector (Fig. A2a), the covariance between each element in the vector was calculated using eq. (12) (Fig. A2b). Generally, for measurements with the same reference epoch, the covariance is positive and highest between measurement pairs whose perturbed epochs are close together in experimental time. The covariance decreases for perturbed epochs far apart in experimental time. Furthermore, for measurement pairs with different reference epochs, the covariance is generally negative when the reference epoch of one pair is the same as the perturbed epoch of another and positive when the perturbed epochs are the same. This shows that if the measurement pairs were considered independent, then the measurements would appear to contain more information than they actually do.

APPENDIX D: DAMPING PARAMETER TESTING

When inverting for the Δt profile within a single coda window (eq. 24), it is important to damp towards the moving reference solution which is a stable solution (eq. 20) to ensure the inverted profile is stable. The measured relative Δt distributions were assumed to follow a multivariate normal distribution, which is only valid for a positive semidefinite covariance matrix. This may not be the case due to errors in the measurement of the covariance matrix. Therefore, to ensure that the covariance matrix is positive semidefinite, we set a minimum correlation coefficient cut-off for valid measurements. This effectively reduced the relative traveltime perturbation matrix (Fig. 7a) to a band of elements around the diagonal. When no damping was applied in the inversion (eq. 24 in main text for $\mu = 0$), the misfit between the predicted and observed relative Δt measurements is high, indicating that the inversion was unstable

(Fig. A3a). The misfit decreases quickly to a local minimum with greater damping, then increases as the inverse solution is further damped towards the moving-reference solution. This indicates that the solution from DLS inversion provides an improvement to the moving reference solution (Fig. A3b). The recorded waveforms show common waveform shapes that can be tracked across epochs (Fig. A3c), which were used to verify that the waveforms have been aligned correctly without cycle skipping, upon correcting for Δt (Fig. A3d)—if the waveforms were aligned incorrectly, this was usually because the moving reference solution contained significant errors and measurements in these coda windows were discarded. Tracking phases in the waveforms across epochs shows how phases appear and disappear throughout the experiment, indicating the importance of measuring Δt locally between epochs close together in experimental time. Moreover, not all phases follow the same Δt profile, due to the heterogeneous distribution of $\Delta v/v$ and differences in path length between phases.

APPENDIX E: SENSITIVITY ANALYSIS

E1 Partial Derivatives of Energy Partitioning Model

The energy partitioning model predicts the traveltime perturbation of the wavefield at a given lapse time with respect to changes in the *P*-wave speed, *S*-wave speed and scattering mean free path traveltime. Relevant notation is given in Table A1; the notation of some variables is different to Appendix B for brevity. We repeat the relevant equations (eqs 16, 17 and B7) here for convenience

$$\Delta t = -t\left[(1-q)\alpha_\Delta + q\beta_\Delta\right], \tag{E1}$$

where

$$q = \gamma^{-1}\left(1-(1-\gamma q_0)\exp\left[-\gamma t\tau_\mathrm{p}^{-1}\right]\right) \tag{E2}$$

and $\gamma = 1+\kappa^{-3}/2$.

To investigate the effects of each parameter on the energy partitioning equation, we can analytically calculate partial derivatives to compare the linearized effect of changes in each parameter. Note that the effect of error in time-zero is captured by the partial derivative with respect to t. For brevity we use the partial derivative notation $\partial_x y \equiv \partial y/\partial x$. The partial derivatives of γ are:

$$\partial_{\kappa_0}\gamma = -3\kappa_0^{-4}(1+\beta_\Delta)^3(1+\alpha_\Delta)^{-3}/2 \tag{E3}$$
$$\partial_{\alpha_\Delta}\gamma = -3\kappa_0^{-3}(1+\beta_\Delta)^3(1+\alpha_\Delta)^{-4}/2 \tag{E4}$$
$$\partial_{\beta_\Delta}\gamma = 3\kappa_0^{-3}(1+\beta_\Delta)^2(1+\alpha_\Delta)^{-3}/2\,. \tag{E5}$$

The partial derivatives with respect to q are:

$$\partial_{q_0} q = \exp\left[-\gamma t\tau_\mathrm{p}^{-1}\right] \tag{E6}$$
$$\partial_\mathrm{t} q = \tau_\mathrm{p}^{-1}(1-q_0\gamma)\exp\left[-\gamma t\tau_\mathrm{p}^{-1}\right] \tag{E7}$$
$$\partial_{\tau_\mathrm{p}} q = t(1-q_0\gamma)\exp\left[-\gamma t\tau_\mathrm{p}^{-1}\right] \tag{E8}$$
$$\partial_\gamma q = -\gamma^{-2}\frac{1+\gamma-q_0\gamma^2 t\tau_\mathrm{p}^{-1}+\exp\left[\gamma t\tau_\mathrm{p}^{-1}\right]}{\exp\left[\gamma t\tau_\mathrm{p}^{-1}\right]}\,. \tag{E9}$$

These partial derivatives are used in conjunction with the product and chain rules to derive the following partial derivatives with respect to Δt:

$$\partial_q \Delta t = t(\alpha_\Delta - \beta_\Delta) \tag{E10}$$
$$\partial_{\alpha_\Delta}\Delta t = t\left(q-1+(\alpha_\Delta-\beta_\Delta)\partial_\gamma(q)\,\partial_{\alpha_\Delta}(\gamma)\right) \tag{E11}$$
$$\partial_{\beta_\Delta}\Delta t = t\left(-q+(\alpha_\Delta+\beta_\Delta)\partial_\gamma(q)\,\partial_{\beta_\Delta}(\gamma)\right) \tag{E12}$$
$$\partial_{\tau_\mathrm{p}}\Delta t = \partial_q(\Delta t)\,\partial_{\tau_\mathrm{p}}(q) \tag{E13}$$
$$\partial_{rmt}\Delta t = (\alpha_\Delta-\beta_\Delta)(q+t\partial_\mathrm{t} q)-\alpha_\Delta \tag{E14}$$
$$\partial_{\kappa_0}\Delta t = \partial_q(\Delta t)\,\partial_\gamma(q)\,\partial_{\kappa_0}(\gamma) \tag{E15}$$
$$\partial_{q_0}\Delta t = \partial_q(\Delta t)\,\partial_{q_0}(q)\,. \tag{E16}$$

In this work, we assume t_0, κ_0 and q_0 to be fixed, and we invert for free parameters α_Δ, β_Δ and τ_p. In reality, there is systematic error on the fixed parameters. We discuss the relative effects of these errors in Section 4.4.

E2 Quality Factor Perturbations

Here, we estimate the effect of changes in attenuation on the estimated wave speed perturbation. At epoch i, let the quality factor be Q_i and the frequency-dependent wave speed be $c_i(\omega)$ where ω is the angular frequency. Consider a constant Q across a frequency band

centred on frequency ω_0. Wave speed is dispersive in attenuative media in order to preserve causality (W.I. Futterman 1962), and is described by the Kramers–Kronig relation:

$$c_i(\omega) = c_i(\omega_0)\left[1 + \frac{1}{\pi Q_i}\ln\left(\frac{\omega}{\omega_0}\right)\right]. \tag{E17}$$

Assuming the only change in the medium is a change in attenuation, that is, $c_i(\omega_0) = c_j(\omega_0)$, the relative change in wave speed between epochs i and j is

$$\frac{\Delta c_{ij}(\omega)}{c_i(\omega)} = \left[\frac{\Delta Q_{ij}/Q_i}{1 + \Delta Q_{ij}/Q_i}\right]\left[\frac{\ln(\omega/\omega_0)}{\pi Q_i + \ln(\omega/\omega_0)}\right], \tag{E18}$$

where $\Delta c_{ij}(\omega) = c_j(\omega) - c_i(\omega)$ and $\Delta Q_{ij} = Q_j - Q_i$.

Given conservative order of magnitude estimates for this experiment of $\ln(\omega/\omega_0) \sim 10^{-1}$, $Q_i \sim 10^1$–10^2, relative quality factor perturbations of $\Delta Q_{ij}/Q_i \sim 10^{-2}$ would produce maximum $\Delta c_{ij}/c_i \sim 10^{-5}$–$10^{-4}$, the sign of which depends on the change in quality factor and the frequency. Given the observed relative wave speed perturbations in this work in the order of 10^{-4}–10^{-3}, estimates of wave speed perturbation due to moderate attenuation perturbations are an order of magnitude less than observed.

E3 Model Parameter Covariance

An analysis of the covariance between model parameters in the energy partitioning inversion model chain (Fig. 10) shows that there is a weak negative correlation between $\Delta\alpha/\alpha$ and $\Delta\beta/\beta$ (Fig. A4a), a weak negative correlation between $\Delta\alpha/\alpha$ and τ_p (Fig. A4b) and negligible correlation between $\Delta\beta/\beta$ and τ_p (Fig. A4c). This is because the coda consists of a mixture between P and S waves so a decrease in the wave speed of one can be made up for an increase in the wave speed of the other for seismic data in coda windows close to equipartitioning.